

# Intrinsic Predictability Limits arising from Indian Ocean MJO Heating: Effects on tropical and extratropical teleconnections

David M. Straus<sup>1</sup>, Daniela I.V. Domeisen<sup>3,4</sup>, Sarah-Jane Lock<sup>2</sup>, Franco Molteni<sup>2</sup>, and Priyanka Yadav<sup>4</sup>

<sup>1</sup>Center for Ocean-Land-Atmosphere Studies, George Mason University, Fairfax, VA, USA

<sup>2</sup>European Centre for Medium-Range Forecasts, Reading, UK

<sup>3</sup>University of Lausanne, Lausanne, Switzerland

<sup>4</sup>Institute for Atmospheric and Climate Science, ETH Zurich, Zurich, Switzerland

**Correspondence:** David Straus (dstraus@gmu.edu)

**Abstract.** Since the Madden-Julian Oscillation (MJO) is a major source for tropical and extratropical variability on weekly to monthly timescales, the intrinsic predictability of its global teleconnections is of great interest. As the tropical diabatic heating associated with the MJO ultimately drives these teleconnections, the ~~effect-of-the~~ variability of heating among ~~various episodes of the same MJO phase~~ ensemble forecasts initialized from the same episode of the MJO will limit this predictability.

5 In order to assess this limitation, a suite of 60-day ensemble reforecasts has been carried out with the ECMWF forecast model, spanning 13 starting dates from 01Nov and 01Jan for different years. The initial dates were chosen so that phases 2 and 3 of the MJO (with anomalous tropical heating in the Indian Ocean sector) were present in the observed initial conditions. The 51 members of an individual ensemble use identical initial conditions for the atmosphere and ocean. Stochastic perturbations to the tendencies produced by the atmospheric physics parameterizations are applied only over the Indian Ocean region. This

10 guarantees that the spread between reforecasts within an ensemble is due to perturbations in heat sources only in the Indian Ocean sector. The point-wise spread in the intra-ensemble (or error) variance of vertically integrated tropical heating  $Q$  is larger than the average ensemble mean signal even at early forecast times; however the planetary wave (PW) component of  $Q$  (zonal waves 1-3) is predictable for ~~24 days for 01Nov starts and 28 days for 01Jan starts. The predictability times, measured by the time at which~~ 25 to 45 days, the time taken for the error variance ~~reaches 0.5 of its saturation value, decreases to 18-20 days for~~ zonal waves 4-10, and 14 days for waves 11-21 to reach 50% to 70% of saturation. This zonal wave 1, the error variance of

15  $Q$  never reaches 90% of saturation. The upper level tropical PW divergence is even more predictable than  $Q$  (40 to 50 days). In contrast, the ~~planetary wave~~ PW component of the 200 hPa Rossby wave source, which is responsible for propagating the influence of tropical heating to the extratropics, is only predictable for ~~14 to 19 days, very close to the predictability times for the 200 hPa vorticity in the 40°N – 50°N latitude belt. In terms of geographical distribution, substantial~~ 20 to 30 days.

20 Substantial ensemble spread of ~~heating and 200 hPa vorticity~~ 300 hPa meridional wind propagates from the tropics to the Northern Hemisphere storm-track regions by days 15-16. Following the growth of upper tropospheric spread in planetary wave heat flux, the stratosphere provides a feedback in enhancing the error via downward propagation towards the end of ~~both Nov. and Jan. the~~ reforecasts.

# 1 Introduction

25 The Madden-Julian Oscillation (Madden and Julian, 1971, 1972) is the dominant mode of tropical variability on subseasonal timescales of several weeks. The MJO manifests as a large-scale convection and precipitation pattern that starts in the Indian ocean, followed by an eastward propagation along the equator. Although the MJO itself is confined to the tropics, it can influence a large part of the globe, including the extratropics, through a wide range of remote impacts, so-called teleconnections (Stan et al., 2017). The best documented teleconnections include impacts on tropical cyclones (Maloney and Hartmann, 2000; 30 Camargo et al., 2019; Hall et al., 2001; Camargo et al., 2009), the North Pacific (Wang et al., 2020), North America (Lin and Brunet, 2009), South America (Valadao et al., 2017), the North Atlantic region (Cassou, 2008; Lin et al., 2009), as well as the upper atmosphere over the Northern hemisphere polar regions (Garfinkel et al., 2014). The mechanisms for an MJO influence on global weather and climate act through the propagation of Rossby waves that are triggered by the diabatic heating anomalies associated with the MJO convection (Sardeshmukh and Hoskins, 1988).

35 MJO teleconnections are a major source of predictability on sub-seasonal to seasonal timescales around the globe (~~Vitart, 2017; Merryfield~~ [\(Vitart, 2017; Merryfield et al., 2020; Stan et al., 2022\)](#)), including for tropical cyclones (Leroy and Wheeler, 2008; Lee et al., 2018; Domeisen et al., 2022), extreme precipitation (Jones et al., 2004; Muñoz et al., 2016), temperature in North America (Rodney et al., 2013), and the Northern Hemisphere stratosphere (Garfinkel and Schwartz, 2017), which in turn can have a strong downward impact on surface weather in the extratropics (Baldwin and Dunkerton, 2001), with strong impacts on 40 extratropical sub-seasonal predictability (Domeisen et al., 2020a).

One class of well-studied ~~teleconnections is that associated with the~~ [tropospheric teleconnections relates to chances in the likelihood of occurrence of the North Atlantic Oscillation \(NAO\)](#). The phase of the MJO with enhanced convection over the Indian Ocean (MJO phases 2 and 3), ~~which tends to be associated with a~~ [is associated with the](#) positive phase of the ~~North Atlantic Oscillation (NAO)~~ [NAO](#) (Lin et al., 2009; Ferranti et al., 1990; Cassou, 2008; Straus et al., 2015) roughly 1-2 weeks 45 later, leading to added predictability (Lin et al., 2010; Vitart, 2014). The ~~teleconnection state of the NAO is also influenced by a~~ [stratospheric teleconnection pathway via upward planetary wave propagation \(Garfinkel et al., 2014; Kang and Tziperman, 2018\)](#). ~~Phases 2-3 (6-7) of the MJO suppress (enhances) the heat flux in the North Pacific region, resulting in a cooler (warmer) polar stratosphere and a stronger (weaker) polar vortex (Garfinkel et al., 2014; Schwartz and Garfinkel, 2020)~~ [The teleconnection of the MJO](#) variability to the NAO is however also modulated by El Niño-Southern Oscillation (Lee et al., 2019), by the propagation speed of the MJO (Yadav and Straus, 2017), and by the strength of the Northern Hemisphere stratospheric polar vortex (Garfinkel and Schwartz, 2017).

Making extended range predictions for mid-latitudes based on an MJO precursor remains challenging (~~Vitart et al., 2017; Schwartz and C~~ [\(Vitart et al., 2017; Schwartz and Garfinkel, 2020; Garfinkel et al., 2022; Stan et al., 2022\)](#)), in part due to the large model errors associated with the teleconnections, ~~both in the tropics and in the extratropics, and in part due to the presence of baroclinic~~ 55 ~~instability and non-linear extratropical interactions such as basic state bias (Schwartz and Garfinkel, 2020; Garfinkel et al., 2022; Stan et al.,~~ [. However, another limitation to predictability is the intermittency of diabatic heating occurring within a single phase of the MJO, and the](#) variability of heating among different [observed](#) episodes of a given phase. ~~In fact, the wealth of MJO~~

teleconnection research discussed above has relied almost exclusively on the Wheeler-Hendon multivariate empirical orthogonal function framework (Wheeler and Hendon, 2004). This framework, by design, involves both spatial smoothing and coarse-graining of the temporal and longitudinal fields of zonal wind and outgoing long-wave radiation, the latter as a proxy for precipitation and thus diabatic heating. Much less studied are the effects on the MJO teleconnections due to the intermittency and variability of the MJO diabatic heating itself, and the intermittency of heating and other sub-grid scale processes in space and time *even within a particular episode*. The dynamical character of the uncertainty in the response to this intermittency has been studied by Kosovelj et al. (2019) in a low resolution global model using idealized stochastic parameterizations. Similarly, the response to model systematic error in Indian Ocean temperatures was addressed by Zhao et al. (2023).

The purpose of this paper is to extend the work of Kosovelj et al. (2019) to address the intrinsic limits of potential predictability due to this uncertainty the intermittency of heating and other sub-grid scale processes in a high resolution operational forecast model setting. In this paper we do not address model systematic error. To this end a series of unique ensemble reforecasts have been carried out that are specifically designed to diagnose the uncertainty in both the tropics and the extratropics that arises due to the high degree of space/time intermittency of diabatic heating sub-grid scale processes within phases 2 and 3 of the MJO. In these reforecasts, made with the Integrated Forecast System (IFS) of the European Centre for Medium-Range Forecasts (ECMWF), the stochastic parametrization scheme (SPPT) described in Leutbecher et al. (2017) has been altered so that perturbations which affect (directly or indirectly) diabatic heating tendencies are confined to the tropical Indian Ocean region. Since all The SPPT alters the instantaneous tendencies of the temperature, specific humidity and horizontal wind components due to sub-grid scale physics processes by scaling these tendencies up or down in a stochastic manner. The physics processes include those due to turbulent diffusion and sub-grid orography, convection, cloudiness and precipitation, and radiation. For more details, consult Leutbecher et al. (2017).

All members of each ensemble use the identical initial conditions, so that the only cause of model uncertainty (also called error here) must be the noise in heating introduced by the SPPT in the tropical Indian Ocean. We should point out here that one might design a similar set of experiments in which only the initial conditions were perturbed. After all, any perturbation whatever to the system will quickly propagate and grow (Ansell et al., 2018). The question is how quickly such errors grow and saturate, and the answer depends on, among other factors, the amplitude of the initial errors. In fact, Zhang et al. (2019) use the this dependence of rate of growth on the magnitude of the initial condition error to estimate the predictability limit of mid-latitude weather. Judt (2018) study the dependence on the rate of initial condition error growth on region (tropical, mid-latitude and high-latitude) for short simulations using a global storm-resolving model.

Another question regarding our experimental design is whether localizing the application of the SPTT to the tropical Indian Ocean is necessary, since following the argument of Ansell et al. (2018), perturbations in any region will quickly propagate to the Indian Ocean region. The only way to answer this question is to re-run the same set of experiments with SPPT applied globally, which is the subject of future research. We will return to this question in the Discussion section.

Since our goal is to document both the uncertainty in the tropical heating and the mid-latitude response in these experiments, we also consider the pathway by which the tropical heating forces extratropical Rossby waves. Although the MJO-related tropical heating is expected to force a corresponding signal in upper tropospheric divergence, this signal generally occurs

within an easterly background wind, where stationary Rossby waves are not expected to propagate. Sardeshmukh and Hoskins (1988) derive a more complete formulation of the source of barotropic Rossby waves ([hereafter Rossby wave source, or RWS](#)) which involves the advection of the absolute vorticity by the divergent component of the flow, and importantly acts in the vicinity of the sub-tropical jet, and so in a background of westerlies. Although strictly speaking the response to the MJO is not stationary, previous success in explaining the extratropical response in terms of stationary wave theory (e.g. Matthews et al., 2004) suggests that stationary wave concepts are relevant here.

Section 2 describes the model and ensemble reforecast experiments in detail, as well as the methods used to diagnose the results. The signal and uncertainty in the tropical heating, ~~and~~ Rossby wave source, ~~and as well as the growth of errors in the tropical~~ circulation on various spatial scales, ~~are described in Section 3, along with the signal and uncertainty in the Rossby Wave Source.~~ Section 4 describes the global spread of error in the ~~heating and~~ circulation and its scale-dependence, while Section 5 shows results related to the stratospheric involvement. The Discussion is given in Section 6, and Conclusions in Section 7.

## 2 Methods and Data

This section introduces the data used in this study, the model experiments performed for this study, and the metrics used to evaluate the data.

### 2.1 Model configuration

This study has been performed using ensemble forecast experiments with the ECMWF Integrated Forecasting System (IFS Cy43r3: see ECMWF (2017a)). The IFS is a global earth system model, which includes an atmospheric numerical weather prediction model coupled to ocean, sea-ice, ocean waves and land surface models. The experiments have been run with the ensemble forecasting system ("ENS") close to the configuration used operationally for the ECMWF extended-range forecasts (<https://www.ecmwf.int/en/forecasts/documentation-and-support/extended-range-forecasts>). This configuration has an atmospheric model resolution of TCo319L91 (approximately 36 km horizontal grid spacing, with 91 vertical levels up to 0.01 hPa, with a timestep of 1200s), coupled to the NEMO ocean model v3.4.1 (Madec and the NEMO team, 2013) in the ORCA025\_Z75 configuration (1/4 degree horizontal resolution, 75 vertical levels), the LIM2 sea-ice model (Goosse and Fichefet, 1999) and the ECMWF Wave Model (ecWAM ECMWF, 2017b). The model system used here is strongly related to the ECMWF extended-range prediction system used for subseasonal to seasonal (S2S) forecasts that is included in the S2S prediction project database (Vitart et al., 2017). This prediction system has been systematically evaluated for its ability to represent MJO teleconnections, along with other prediction systems from the S2S database ([Vitart et al., 2017](#); [Stan et al., 2022](#)) ([Vitart et al., 2017](#); [Stan et al., 2022](#)). Overall, the ECMWF system reproduces a realistic teleconnection to the Northern Hemisphere, though with a too weak amplitude. Among the models investigated in the above studies, the ECMWF system exhibits a skillful representation of the MJO teleconnections. ~~Hence using the ECMWF system to study error growth from MJO teleconnections allows for an identification of remaining issues at a state-of-the-art level of model development.~~

## 125 2.2 Description of ensemble reforecasts

Ensemble reforecasts were made for initial dates of 01 Nov and 01 Jan, but only for those years (between 1981 and 2016) when the MJO resided in phases 2 or 3 with an amplitude greater than 1.0 on the initial date. From the MJO amplitude and phase data from the Australian Bureau of Meteorology (<http://www.bom.gov.au/climate/mjo/>), this condition yielded eight years for the Nov reforecasts and five for the Jan reforecasts. The dates are given in Table 1.

130 All members of each ensemble forecast are initialized with *identical* initial conditions from the ERA-Interim reanalysis data (Dee and coauthors, 2011). There are no perturbations applied to the initial conditions. The ~~control~~-single control forecast for each initial date also has no perturbations applied during the integration. The 50 additional members of each ensemble forecast differ only in that perturbations are applied during the model integrations. These are introduced via the operational model uncertainty scheme, SPPT (Stochastically Perturbed Parametrization Tendencies scheme, see Leutbecher et al., 2017; 135 Buizza et al., 1999). SPPT is designed to represent model uncertainty due to the parameterization of atmospheric physical processes. In ECMWF’s operational forecasts, SPPT perturbations are applied at every time step of the runs and at every grid-point over the entire globe. However, for these experiments, a mask is applied such that the SPPT perturbations are only active within a window over the Indian Ocean, i.e. they are fully active in (50E – 120E, 20N – 20S) and tapered to zero within the neighbouring 5 degrees (in all directions). All the forecasts are run to a lead-time of 60 days.

140 In addition, 01 Nov and 01 Jan ensemble reforecasts were made for all years between 1981 and 2016 with the initial dates of 01 Nov and 01 Jan. Here the ensemble size is 9, with a control (unperturbed) run and 8 perturbed runs. The purpose of these ‘all-year’ reforecasts is to establish the model reforecast seasonal cycle for the Nov-Dec and Jan-Feb periods. Table 1 summarizes the MJO and all-year reforecasts, while Table 2 gives the MJO amplitude and phase for each of the reforecasts of Table 1. In addition, Table 2 gives the monthly mean Niño 3.4 indices to indicate the state of the El-Niño Southern Oscillation. 145 (This index is defined as the sea-surface temperature averaged over the region  $5^{\circ} - 5^{\circ}N$  and  $170^{\circ}W - 120^{\circ}W$ , and was obtained from the website <https://www.cpc.ncep.noaa.gov/data/indices/>) Note that there are four 01 Nov start dates (for 1986, 1987, 2002 and 2015) which occur during a warm ENSO event, defined by having the Niño 3.4 index close to or above 1.0 for both forecast months. For the 01 Jan start dates, only 1987 and 2010 occurred during warm events. Since we will consider the diabatic heating throughout the tropics, the state of ENSO, which impacts the heating in the central Pacific is relevant.

150

## 2.3 Data and diagnostics

The output of the 60-day forecasts includes the fields of temperature  $T$ , geopotential height  $Z$ , horizontal winds  $(u, v)$  and vertical pressure velocity  $\omega$  at 12 pressure levels: 1000, 925, 850, 700, 600, 500, 400, 300, 250, 200, 100, 50  $hPa$ . These fields 155 were available twice-daily on an N80 Gaussian ( $320^{\circ} \times 160^{\circ}$ ) lon x lat grid.

The diabatic heating was computed as a residual in the thermodynamic equation, with resolution equivalent to T159 in spherical harmonic space, following the algorithm described in Swenson and Straus (2021). While the output of the algorithm

**Table 1.** Summary of the model runs performed for this study, for the November start dates (left) and the January start dates (right).

Start date	Ensemble size	Start date	Ensemble size
01 Nov 1986	50+1	01 Jan 1987	50+1
01 Nov 1987	50+1	01 Jan 1990	50+1
01 Nov 1990	50+1	01 Jan 1995	50+1
01 Nov 2001	50+1	01 Jan 2010	50+1
01 Nov 2002	50+1	01 Jan 2013	50+1
01 Nov 2004	50+1		
01 Nov 2011	50+1		
01 Nov 2015	50+1		
01 Nov 1981..2016	8+1	01 Jan 1981..2016	8+1

**Table 2.** Values of MJO amplitude and phase for the initial date of each reforecast ensemble, and observed monthly mean Niño 3.4 index for the two months of each reforecast ensemble. The index is only reported for absolute values above 1.0.

<b>MJO Amplitude and Phase</b>				
Start Date	MJO Amp	MJO Phase	Nino3.4 Nov	Nino3.4 Dec
01 Nov 1986	2.77	3	1.01	1.12
01 Nov 1987	1.58	2	1.07	0.94
01 Nov 1990	1.76	3		
01 Nov 2001	1.56	3		
01 Nov 2002	1.96	2	1.47	1.37
01 Nov 2004	1.32	3		
01 Nov 2011	1.11	3	-1.19	-1.06
01 Nov 2015	2.04	3	2.72	2.66
Start Date	MJO Amp	MJO Phase	Nino3.4 Jan	Nino3.4 Feb
01 Jan 1987	1.22	2	1.14	1.13
01 Jan 1990	1.07	3		
01 Jan 1995	1.41	3	1.02	
01 Jan 2010	1.72	3	1.52	1.25
01. Jan 2013	1.07	3		

yields the heating in  $Wm^{-2}$  integrated over three layers:  $1000 - 850 hPa$ ,  $850 - 400 hPa$ ,  $400 - 50 hPa$ , in this paper we ~~only show the present diagnostics from both the mid-level ( $850 - 400 hPa$ ) heating  $Q_{mid}$  and the full vertical integral spanning~~  
 160  $1000 - 50 hPa$ , ~~which we refer to as heating  $Q$~~ . The daily mean diabatic heating from the ERA5 reanalysis (Hersbach and coauthors, 2020) was computed from the same fields, sampled four times per day, for the Novembers of the eight years listed in Table 1.

~~The effective barotropic~~ The Rossby wave source was computed following the prescription of Sardeshmukh and Hoskins (1988) as:

$$165 \quad S = -\nabla \cdot \left( v_{\chi} \zeta_a \right) \quad (1)$$

where  $\zeta_a = f + \zeta$  is the absolute vorticity, and ~~the vector~~  $v_{\chi}$  the divergent component of the horizontal flow vector. ~~This was evaluated at the 200 hPa level, using model fields at an equivalent T21 spectral truncation. The final result was also truncated to~~ In order to compute  $S$ , we made use of the following transforms between the Gaussian grid and spherical harmonic (spectral) representations: Here  $(u, v)$  are the horizontal components of any vector on the grid,  $(\hat{D}, \hat{V})$  are the corresponding  
 170 divergence and curl in spectral representation, and  $F$  is the grid point representation of any scalar field and  $\hat{F}$  its representation in spectral space. Applying transform ?? to the horizontal flow vector gives the ordinary divergence and vorticity in spectral space; transform ?? then yields the relative vorticity  $\zeta$ . To obtain the vector  $v_{\chi}$  we apply transform ?? using the spectral divergence  $\hat{D}$  obtained from the horizontal winds but setting  $\hat{V} = 0$ . Finally we use ?? on the vector  $(u_{\chi} \zeta_a, v_{\chi} \zeta_a)$  to obtain the corresponding divergence  $\hat{S} = \hat{D}$  in spectral space, followed by at transform back to  $S$ . In applying this last transform, only  
 175 spectral components corresponding to T21 ~~and were retained, and the final field was~~ averaged over two-day blocks.

In order to consider the source outside the deep tropics (where the background easterlies would suppress a stationary wave response) and in the vicinity of the sub-tropical jet, we consider the average source between  $15^{\circ}N$  and  $30^{\circ}N$ . The final values were divided by  $\frac{2\Omega}{a}$ , where  $\Omega$  is the angular rotation rate of the earth, and  $a$  the radius of the earth. The scaled values have units of  $\frac{m}{s}$ . ~~Details regarding the calculation of the Rossby wave source are given in the Appendix. The results shown in this paper~~  
 180 ~~are robust to changes in the latitude band chosen, both to modest poleward displacement and to widening it by 5 degrees.~~

## 2.4 Definition of anomalies

The seasonal cycles corresponding to the Nov. and Jan. MJO experiments listed in Table 1 are computed from the corresponding all-year experiments, and are characterized by a single climatological parabola in time for each variable and grid point, as in Straus (1983). Deviations in time about this seasonal cycle give the anomalies.

## 185 2.5 Metrics of uncertainty

Several metrics of the growth in uncertainty ~~due to the small perturbations in the initial conditions~~ are used in this paper. In all cases what is measured is the uncertainty due solely to the spread of each ensemble with forecast time, without any reference to reanalysis or observations. The *internal error variance* is defined as the average squared difference of a variable between the perturbed reforecasts ~~(to which SPPT has been applied)~~ and the control reforecast for the same initial date, ~~and gives a~~

190 ~~measure of the “perfect model” error.~~ The *ensemble error variance* is defined as the average of the squared difference between the perturbed reforecasts and the ensemble mean. Its square root is referred to as the ensemble spread. Finally, the *external error variance* is defined as the average of the squared difference between each reforecast of one ensemble and all the control forecasts from the all-year experiments. The external error variance gives a simple measure of the saturation level of the internal error variance. This saturation level will depend on time due to the evolution of the seasonal cycle.

195 Note that the error variances of the kinetic energy are just the sum of the corresponding error variances of the components of the horizontal winds  $(u, v)$ , divided by 2. Thus  $var_{KE} = \frac{1}{2}(var_u + var_v)$ .

### 3 Results

#### 3.1 Tropical signal

~~Although all eight (five) initial conditions for 1 Nov. (1 Jan.) for our experiments occur within MJO phases 2-3 (with a normalized amplitude greater than 1.0), the evolution of the tropical heating anomalies is quite variable from experiment to experiment. This is illustrated in Figure 1 (for the Nov experiments) and Figure ?? (for the Jan experiments). The daily averaged evolution of vertically integrated diabatic heating anomaly is shown averaged for the first 30 days of the 60-day experiments in Figure 1c. The heating has been averaged over the tropical band (15S-15N) and, over all ensemble members and all four 01 Nov experiments during warm ENSO events (1986, 1987, 2002 and 2015) in Figure 1(a), and over all experiments. The eastward propagation of positive heating anomalies near longitude 90E can be seen for about 8 days, along with robust westward propagation of heating anomalies that appear after 4 days in the central Pacific. The ensemble spread of the heating (also averaged over the four remaining 01 Nov experiments (1990, 2001, 2004 and 2011) in Figure 1(b). The average over all 8 Nov experiment tropical band and all experiments) is shown in Figure 1(e). The propagation of the heating corresponding to the MJO is seen clearly in each of the averages, but with a distinct difference. During non-ENSO years (Figure 1(b)), the diabatic heating envelope propagates from 90°E to 120°E in about 7 days and reaches the dateline by day 10. In contrast, during the warm ENSO years (Figure 1a) the main envelope of heating propagates slightly westward initially and then starts its eastward propagation only around day 6. A weaker secondary branch of heating is also seen propagating eastward around day 3. After day 10, d. The dominant influence of the SPPT generated perturbations over the Indian Ocean sector is clear, leading to the ENSO heating anomaly in the eastern Pacific dominates. The heating anomaly averaged over all experiments (Figure 1e) tends to wash out these two distinct signals.~~

200  
205  
210  
215

~~For the January experiments, the non-ENSO years (Figure ??b) show a strong eastward moving envelope of largest ensemble spread in this sector.~~

~~In order to gauge the degree of influence of ENSO on the heating which takes about 12 days to reach the western Pacific but then spreads rapidly to the dateline by around day 14. In the Indian Ocean, the eastward propagating envelope of heating consists of two westward propagating sub-branches. Strong westward propagation is also seen initiated in the eastern Pacific Ocean. The warm ENSO event average heating anomalies shown in Figure ??a are perhaps the most interesting: The Initially westward propagating envelope turns eastward around day 6 and then jumps to the eastern Pacific by day 9, with subsequent rapid~~

220



propagation to join the main ENSO-related heating anomalies around 160°W. Meanwhile, a second MJO episode is seen to develop in the western Indian Ocean at day 10, propagating rapidly into the eastern Pacific. For the January experiments, the average over all experiments (Figure ??c) shows a distinct eastward propagating envelope, with westward propagating sub-components evolution, we also show the tropical heating anomalies separately for the six warm ENSO events (Nov 1986, Nov 1987, Nov 2002, Nov 2013, Jan 1987, Jan 2010) in Figure 1a and for the remaining seven experiments in Figure 1b. The warm events show the establishment of strong tropical heating in the central Pacific after day 15 (as expected), while both sets of years show robust westward propagation of the heating from the central Pacific. The initial eastward propagation of the Indian Ocean anomalies is somewhat delayed in the warm event years in comparison to the neutral years.

Figure ??2 shows the evolution of both the ensemble average and ensemble spread of the Rossby wave source  $S$  averaged over all Nov. experiments (Figure ??a) and all Jan. experiments (Figure ??b) for of the first 30 days. latitudinally averaged RWS, averaged over all experiments, for the first 30 forecast days. Figure 2a) shows the results for averaging over latitudes 15°N - 30°N, while 2b) shows the results for latitudes 20°N - 35°N. In both cases, coherent eastward propagation of a dipole pattern is seen over the first 10 days (although the magnitude of the RWS is larger for the band that extends to 35°N.) This pattern straddles the location of the largest mean heating seen in Figure 1c. Beyond forecast day 30, the mean signal in RWS shows little propagation (not shown).

The colors indicate where the signal-to-noise ratio  $\sigma$ , defined as the the ratio of the mean ensemble average to mean ensemble spread, is greater than 1.0 or (for positive RWS) or less than -1.0. Figure ??a shows that  $S$  takes the form of a dipole (between 50°E and 90°E), which propagates eastward with  $\sigma > 1$  for up to (for negative RWS). This ratio shows that the propagation of the RWS is coherent (with the magnitude of the signal-to-noise ratio exceeding 1.0) for the first 8 to 10 days, similar to the time scale of coherent propagation of  $Q$  seen in Figure 1. A similar dipole is seen for January (Figure ??b), with an additional coherently propagating episode of large  $S$  seen after day 12. This second episode, with  $\sigma < 1$  corresponds to a similar one for the El-Niño cases shown in Figure ??a forecast days.

### 245 3.2 Tropical error growth

The daily averaged ensemble spread of vertically integrated heating  $Q$ , averaged over all November-January experiments, is shown in Figure 1d Figure ??d. The spread develops quickly at the same longitude as the average heating anomalies, 80°—90°E in November and 90°E in January, but with a somewhat larger magnitude. Note that the color bar scale is different for the ensemble spread than for the anomalies. The. During the first few days, the heating spread grows substantially between longitudes 90° and 95° in the Indian Ocean during the November experiment, as expected since the stochastic perturbations are applied this region, precisely where the mean heating is greatest. The values of the maximum spread decrease after about 6 days, but large spread is seen over a wider area as the uncertainty propagates. (Note for reference that the longitudinal boundaries of the applied SPPT perturbations are indicated by the faint vertical red lines in Figure 1b.)

In order to determine whether the strength of the stochastic perturbations (reflected in the magnitude of the ensemble spread in the Indian Ocean region) is reasonable, we also computed the the inter-annual standard deviation of the November  $\sigma_{JA}$  of the tropical  $Q$  from the ERA5 reanalysis over the eight years corresponding to the Nov. Experiment for the first 30 days. Figure

A1 in the Appendix shows the daily evolution of the standard deviation with the same scale as in Figure 1d. In the The ERA5  $\sigma_{IA}$  is largely confined to the same regions as the model spread: the Indian Ocean region and the west-central Pacific. In the two fields are comparable.

260 The spread in January, having developed quickly in the Indian Ocean, becomes (after day 10) intense at the eastern edge of perturbation region (around  $120^{\circ}E$ ) following the average heating anomaly. For both cases, the spread also develops in the central Pacific, following to some extent the average heating. sector, the model spread in heating has somewhat lower maximum values than  $\sigma_{IA}$ , but extends over a wider area. The model spread is notably less than  $\sigma_{IA}$  over the Pacific up to forecast day 30.

265 In order to investigate the scale-dependence of the uncertainty of the heating evolution, we calculated the evolution of the zonal wavenumber spectra of the internal error variance of (two-day averaged)  $Q$  over  $Q_{mid}$  ( $850 - 400 hPa$ ) averaged over 2-day blocks and over the tropical belt  $15^{\circ}S - 15^{\circ}N$ . Since it is expected that very small-scale differences in  $Q$  will not contribute significantly to the global response, we have smoothed the heating by retaining only scales consistent with a T21 spherical harmonic representation prior to computing the error variances. The zonally averaged variances are decomposed into  
270 contributions due to groups of zonal wavenumber  $m$ . Figure ??a shows the evolution of the error variances of  $Q$  averaged over all Nov. experiments. The internal variance is shown by the black curves, the external error variance by the blue curves and the ensemble error variance by the red curves. Results are shown for various groups of zonal wavenumber: 1—3 (top panel), 4—10 (middle panel) and 11—21 (lower panel). The results for the Jan. experiments are given in Figure ??b. The large-time limit of the internal error is seen to be about twice that of the ensemble error variance. Figure 3 shows the spectra for the blocks  
275 ending on days 2, as expected.

For the planetary waves ( $m = 1 - 3$ ), 4, 6, 10, 20, 40 and 60. The latter is indicated by the internal error stays well below our estimate of red line, and gives a simple measure of saturation. By day 2, the spectrum is relatively flat down to length scales of about 3000 km, consistent with the variance being forced by perturbations in a narrow longitude range. As time progresses, the variance increases without dramatic change in shape until after day 20, when the larger scales (wavelengths greater than  
280 about 3500 km) grow more rapidly than the smaller scales, leading to a steeper variance spectrum by 60 days. If we define the predictability time  $\tau$  to be the time it takes for the error variance to reach a given fraction of saturation,  $\tau$  increases with length scale.

To make this more precise, we show the the time  $\tau$  at which the error variance of  $Q$  reaches a fraction  $f_{\tau}$  of the variance of the external error for 30 days and beyond, but at this forecast range the saturation of the internal error is almost complete  
285 for  $m = 4 - 10$ . The internal error variance for smaller scales  $m = 11 - 21$  reaches the external error variance prior to day 30. These observations hold for both Nov. and Jan. experiments, and also hold for the ensemble error variance, which particularly in the Nov. experiments is still growing, albeit slowly at day 60.

It is instructive to normalize the internal error variance shown in Figure ?? by the corresponding external error variance for each forecast time. The resulting normalized error variance (shown by the black lines in Figure ??) approach and hover about  
290 1.0 at large times for all wavenumber groups except  $m = 1 - 3$ , for which the error does not appear to have saturated even at day 60. In order to summarize the  $f_{\tau} = 0.50, 0.70, \text{ and } 0.90$ , as a function of zonal wavenumber in Figure 4a. The red curves

give the results for  $Q$  in the solid, dashed and dotted lines, respectively. Prior to calculating the error growth characteristics in a way which allows comparison between experiments, wave groups and variables, we define a predictability time variances for this plot, we have truncated  $Q$  (and the other fields to be shown) to a spherical harmonic T21 representation in order to eliminate excessive noise.  $\tau$  as the time it takes for the normalized internal error to reach 0.5, as indicated by the light black horizontal lines in Figure ???. The rate of internal error growth vis-a-vis the external error (saturation) can then be summarized by the single measure  $\tau$ , which allows for easy comparison between different variables and regions.  $\tau$  increases with zonal scale (decreasing wavenumber) for all choices of  $f_\tau$ , but this is particularly noticeable for  $f_\tau = 0.70$  and  $0.90$ . In fact the limit of  $0.90$  of the external error is never reached for zonal wavenumbers 1 and 2.

The predictability times for the vertically integrated heating  $Q$  (averaged  $15^\circ S - 15^\circ N$ ) and the 200 hPa T21 representation of the upper-level (200 hPa) divergence are shown in Figure 4b in the blue curves. These times are notably longer than for the vertically integrated heating. For example, the divergence  $\tau$  corresponding to  $f_\tau = 0.70$  is greater than 35 days for the largest scales, compared to 20 days for the heating  $\tau$ . While this might be taken to indicate high predictability for the extra-tropical response, the corresponding times for the Rossby wave source  $S$  (averaged  $15^\circ N - 30^\circ N$ ) are given in Table ?? for the three wavenumber groups and for both Nov. and Jan. reforecasts. The  $\tau$ , shown in the blue curves in Figure 4b, are considerably shorter than those for  $Q$ . This is especially true for the planetary waves (wavenumbers 1 - 3) for which the predictability time for the planetary wave Rossby wave source  $\tau_S$  is considerably shorter than that for the heating  $\tau_Q$  in both Nov. (14 vs. 24 days) and Jan. (19 vs. 28 days). As the zonal scale decreases (larger  $m$ ),  $\tau$  generally decreases, and  $\tau_S$  approaches  $\tau_Q$  by about 8 days for  $f_\tau = 0.50$ , and by about 10 - 20 days for  $f_\tau = 0.70$ . This reflects the sensitivity of the RWS to the sub-tropical divergent flow and also the sub-tropical absolute vorticity (as expressed in equation 1). The predictability times for the RWS have not, to our knowledge, been shown before, and are an important result regarding the predictability of the extra-tropical circulation.

### 3.3 Global error growth

Predictability Times based on normalized external error variance growth for vertically integrated heating averaged between  $15^\circ S - 15^\circ N$ , and 200 hPa Rossby wave source averaged between  $15^\circ N - 30^\circ N$ . 1-3 24 14 28 19 4 10 18 14 The forecast evolution of the spectra of the internal error variance of kinetic energy (KE) is presented in Figure 5 for different latitude bands. In the tropics ( $15S - 15N$ ; Figure 5d), the spectra grow without much change in shape between forecast days 3 and 10, but between days 10 and 20 for smaller scales approach saturation much more quickly than do the larger scales. Wave lengths shorter than about 3500 km are already saturated by day 20, while the larger scale error variance continues to grow beyond day 40. The times for which the spectra are shown in Fig. 5d (3, 5, 10, 20, 40 and 60 days) are the same as in the other panels (Figs. 5a - 5c), which show latitude bands of  $25N - 35N$ ,  $45N - 55N$  and  $65N - 75N$ , respectively. As one goes to higher latitudes (i.e. from panels (c) to (b) to (a)), the error variance curve for days 3 and 5 continuously moves to lower values, indicating the time it takes for the error to propagate poleward from the tropics. However by day 40, the curves are at about the same level for all latitudes except the  $65N - 75N$  band, where the error is less than at other latitudes. In fact the saturation error (estimated by the red curve at day 60) is also less.

Predictability Times based on normalized external error variance growth for 200 hPa vorticity in the regions  $15^{\circ}S$ — $15^{\circ}N$  (“Tropics”) and  $40^{\circ}N$ — $50^{\circ}N$  (“Mid-Lat”). 1-3 20 15 23 19 4 10 16 15 19 16 11 21 14 12 16 14

### 3.4 Global error growth

To get a sense of how the errors spread geographically, we present maps of the ensemble spread in vertically integrated heating  $Q$  for various forecast ranges up to day 30 in Figure ?? for the Nov. experiments, and in Figure ?? for errors spread geographically, we present maps of the ensemble spread of the meridional wind in Fig. 6. The choice of meridional wind was motivated by its close relationship with storm tracks and circumpolar wave guides (Branstator and Teng, 2017). Much of the tropics outside of the Indian Ocean region is nearly error free even at day 6. By day 10, substantial error has already appeared in the extra-tropics, particularly in the storm-track regions, and by day 16 the Jan. experiments. In November, the spread is largely confined to the Indo-Pacific region through days 5-6, begins to propagate into the northern hemispheric storm track regions by days 9-10, and by days 15-16 is well established in the North Pacific and Atlantic Oceans (and also the sub-tropical southern hemisphere oceans). Beyond forecast day 15, and up to Day 30, the errors intensify but retain a similar distribution. The spread in heating in the Jan. experiments follow a similar evolution. However by Day 30 a noticeable hemispheric asymmetry is present, with much stronger errors in the southern hemisphere.

In considering the evolution of the ensemble spread of vorticity, we have retained only scales consistent with a T21 spherical harmonic representation, consistent with the treatment of heating. The evolution of the spread in vorticity at 200 hPa shown in Figures ?? and ?. It is clear that the vorticity ensemble error grows more quickly in the extratropics than the tropics. As with the heating, the errors begin to propagate into mid-latitudes by forecast days 9-10 and are well established in the storm track regions of both hemispheres by days 15-16, after which they amplify. Noteworthy is the hemispheric asymmetry for Nov., with the northern hemisphere errors dominating at day 30. extra-tropical spread has almost saturated. By day 30 the spread in the extra-tropics has essentially reached its saturation value, since it doesn't increase for longer lead times (not shown).

### 3.4 Error propagation through the stratosphere

Since the stratosphere plays a dominant role in role in the teleconnections from the tropics as a modulator for extratropical long-range forecasts (e.g. Domeisen et al., 2015), we next evaluate the role of the stratosphere in error propagation. Since the polar vortex tends to form in mid- to late-winter (Balwin and Holton, 1988) we present results for the Nov. and Jan. reforecasts separately. The ensemble error variance of the zonal wind  $u$  was integrated over the polar cap ( $60^{\circ}N$ — $90^{\circ}N$ ), and the contributions to the zonal mean error variance from errors in the zonal flow and zonal wavenumbers  $m = 1 - 3$  computed. The corresponding spread (square root of the variance) is shown in Figures ??a and ??7a and 7b for the November initializations, and Figures ??e and ??7c and 7d for January, at levels from 1000—50 hPa. Some evidence for the downward propagation of errors (in the form of ensemble spread increasing from the top, i.e. from 50 hPa) from the stratosphere appears during the last 10 days of the November experiments, and slightly earlier in the January initializations, in both the zonal mean and planetary wave contributions. This downward propagation is potentially linked to wave-mean flow interaction which acts to bring anomalies in e.g. wind and temperature to the lower stratosphere. The planetary wave error in the upper troposphere (300 hPa)

~~for Nov. reaches a maximum 20 days earlier than does the error at 50hPa, hinting at a tropospheric forcing of the stratospheric spread.~~

360

The upward propagation of the wave activity from the upper troposphere into the stratosphere, as measured by the vertical component of the Eliassen-Palm flux, is proportional to the zonal mean of the meridional eddy heat flux. Thus we would expect that if the spread in the tropospheric planetary wave activity is responsible for the growing ensemble error in the stratosphere, we should see evidence for this in the spread in the heat flux, especially in the contribution from zonal wavenumbers  $m = 1 - 3$ .

365

Figure ??8 shows this heat flux as a function of time and pressure level for both Nov. and Jan. experiments. For Nov., enhanced spread in the eddy heat flux is seen by day 30, and by day 40 this spread has grown in the stratosphere. This occurs even earlier (by 10 days) in the Jan. experiments, likely due to the stronger wave flux into the stratosphere and hence a stronger upward coupling. For the Nov. experiments (Figure ??8a), the spread increase in the upper troposphere is seen slightly prior to its increase in the stratosphere, although for the Jan. experiments the increased spread in the troposphere and stratosphere tends

370

to occur nearly simultaneously.

In order to better understand the longitudinal dependence of the upward error growth, the geographical distribution of the planetary wave heat flux at 50 hPa is described in Figure ??9. This figure shows both the ensemble mean eddy heat flux due to  $m = 1 - 3$  and the ensemble spread, whose zonal mean is depicted in Figures ??8a. and ??8b. The four rows give pentad time averages for pentads 1, 3, 5 and 7. The heat flux itself is largely confined to the North Pacific in the ensemble mean, which is the region of upward propagation of planetary waves from troposphere into the stratosphere in the MJO teleconnections (Schwartz and Garfinkel, 2020) but other high latitude regions contribute substantially to the spread. This is true particularly for the Jan. experiments (columns 3 and 4), in which large values of the spread are seen over the entire belt around  $60^\circ N$  by pentad 5 (forecast days 21-25). The analysis of geopotential height spread at 500hPa in the North Pacific sector (not shown) gives similar results.

375

## 380 4 Discussion

The evolution of tropical heating ~~averaged over all Jan. (Nov.) experiments in Figure 1 c (??e) shows a strong maximum initially followed by eastward propagation with a reduced amplitude. The apparent decay of this average heating signal in time is due partly to the variation in the detailed evolution in the ensemble mean heating for the different initial dates. (Note that we also have included one MJO phase-2 case for Jan., and two MJO phase-2 cases for Nov. in shown in Figures 1 for~~ El-Niño years shows less eastward propagation from the Indian Ocean compare to normal years, in line with the findings of Liu et al. (2020), likely because less moisture is available over the Indian Ocean due to the grand-average ENSO convection in the central Pacific. Nevertheless, the average over all forecasts does show distinct eastward propagation for the first 10 days or so. The Rossy Wave Source shown in Figure 2 shows a corresponding propagating signal over the broad Indian Ocean region for the first 10 days.

390

~~An indication of the variability among the ensemble members is the large ensemble spread of heating shown in Figures 1d and ??d. The very large initial uncertainty is confined to a narrow longitudinal range, but propagates in longitude with~~

time as expected. In spite of this large local error in  $Q$ , the planetary wave component error grows much more slowly, with a predictability time  $\tau_Q$ . The evolution of the average of the ensemble spread in vertically integrated heating ( $\Delta Q$ ) shown in Figure 1d shows clearly that the within-ensemble variability induced by the application of the regionally confined SPPT remains mostly confined to that region ( $50^\circ - 120^\circ\text{E}$ ) for the first 10 days or so. This is also true for the tropical meridional wind spread (Figure 6) for the first 6 days. This suggests that the evolution of the tropical heating and circulation uncertainties would be different had the SPPT been applied throughout the tropical belt. Whether this difference would strongly affect the growth of uncertainty in the extra-tropics is hard to assess directly from these experiments. This question awaits future research.

Consistent with the tropical  $\Delta Q$  remaining somewhat regionally confined, its spectrum is relatively flat over a range of 24 days for Nov. and 28 days for Jan. scales for the first 20 days or so (Figure 3), with the error growth similar for different scales. However, after day 20 scales less than a few thousand km. approach saturation, while the largest scales remain far from saturation. Here the saturation spectrum (given by the red line), defined as the error after 60 days, has become steeper, with the largest scales having the greatest variance.

The corresponding times predictability times  $\tau$ , shown in Figure 4, reveal an interesting result: The upper-level tropical divergence, largely forced the tropical heating, is far more predictable than the heating, with the largest scales reaching 0.50 (Figures ?? and ?? and Table ??). In fact the planetary wave internal error variance of  $Q$  does not fully saturate over the course of the experiments. The relatively long predictability times for tropical planetary wave heating are reflected in 0.70 of their saturation level only near day 40 (50). Clearly the upper-level divergence is relatively insensitive to the details of the heating.

A naive interpretation of the tropical divergence as the main forcing function for the extra-tropics would indicate long-range predictability related to the predictability times for the tropical circulation as seen in Table ??, which are longer than their mid-latitude counterparts, consistent with earlier studies, for example Straus and Paolino (2009). Such long times justify the approach of, for example, Matthews et al. (2004) in using stationary wave concepts to describe the extratropical response to the MJO.

Although the largest scale heating and circulation components are predictable out to 3 weeks in these experiments, they do not directly force the extratropical response. Rather, the forcing is encapsulated in the Rossby wave source. However, the predictability times for the Rossby Wave Source  $S$  are considerably shorter: the largest scales reach 0.50 (0.70) of saturation already at around 20 (30) days. This is understandable since  $S$  is influenced not only by tropical and subtropical divergence but also by the meridional gradient of the jet, it is not as predictable as the heating (with  $\tau$  reduced by about by 10 days, as seen in Table ??). This result indicates that one. One path by which mid-latitude and sub-tropical variability may affect the response to tropical forcing is by changing the effective source for that response. Nevertheless, predictability times for  $S$  of 20 - 30 days are long enough to justify the approach of, for example, Matthews et al. (2004) in using stationary wave concepts to describe the extratropical response to the MJO. One path by which mid-latitude and sub-tropical variability may affect the response to tropical forcing is by changing the effective source for that response. The two-week predictability times for  $S$  are also consistent with the spread of vorticity and heating uncertainty to the storm track regions during that time, as seen in Figures ??, ??, ?? and ??.

430 The slopes of the saturation (or background) kinetic energy spectra presented in Figure 5 are compared to those corresponding to a dimensional wavenumber dependence of  $k^{-3}$  and to a dependence of  $k^{-5/3}$  in indicated by dashed and solid lines in the Figure. (The dimensional wavenumber  $k = \frac{2\pi}{\lambda}$  with  $\lambda$  being wavelength.) A slope corresponding to a  $k^{-3}$  dependence is evidence of the dominant of rotational flow, while a  $k^{-5/3}$  dependence is associated with the dominance of convection and gravity waves, and in general divergent flow (Charney, 1971; Sun et al., 2017; Zagar et al., 2017; Li et al., 2023).

435 Our tropical saturation spectrum, showing a  $k^{-3}$  dependence, is in distinct contrast to that of Jutd (1988) (their Figure 5), which shows a slope roughly corresponding to a  $k^{-5/3}$  dependence, indicative of the dominance of convection and divergent flow. In mid-latitudes, the background spectrum of J also shows a transition from a  $k^{-3}$  to a  $k^{-5/3}$  dependence at several hundred km., a transition our results are unable to resolve. These differences are due to the model resolution and dynamics, as J uses 4-km horizontal resolution, storm-resolving simulations without convective parameterizations, while the IFS model used here has a resolution of 36-km and makes use of parameterizations for unresolved processes. Similar to the spectra shown in Zhang et al. (2019) (their Figure 6), the mid-latitude error growth is rapid between days 5 and 10, while the continued error growth for the largest scales at later times is similar to that reported in Selz (2019) in their Figure 4, noting that the spectra are  
440 plotted differently.

The growth of uncertainty in the stratospheric circulation, as seen in Figure ??7, is forced by the upward propagation of the planetary wave meridional flux of sensible heat (which is the dominant term in the vertical component of the Eliassen-Palm flux), shown in Figure ??8. This uncertainty then propagates downward into the upper and middle troposphere. While most of the upper troposphere sensible heat flux is due to planetary wave disturbances in the Pacific, its uncertainty in the North Atlantic and Asian sectors are also large, especially for the Jan. experiments (Figure ??-9). This downward propagation is potentially  
445 linked to wave-mean flow interaction which acts to bring anomalies in e.g. wind and temperature to the lower stratosphere. The planetary wave error in the upper troposphere (300hPa) for Nov. reaches a maximum 20 days earlier than does the error at 50hPa, hinting at a tropospheric forcing of the stratospheric spread.

The stratospheric descent of error seen in Figure ??-7 occurs towards the end of the experiments, consistent with the tropo-  
450 spherically forced uncertainty being modulated by the stratospheric circulation (Domeisen et al., 2020b). This descent is seen about 10 days later in the reforecast period for the Nov. experiments than for the Jan. experiments. This may-be-is likely due to the lack of a fully formed stratospheric vortex during November, so that the establishment of a wave guide for vertically propagating Rossby waves is delayed. (It was not possible to verify this since data were retained only up to 50hPa.)

## 5 Conclusions

455 The suite of reforecast-ensemble-ensemble reforecast experiments presented here was explicitly designed to gauge the effect of the uncertainty-in-the-diabatic-heating-within-MJO-intrinsic uncertainty of sub-grid motions on the response to the MJO in phases 2 and 3 on the global circulation. We-3. Each ensemble has all its members initialized identically during an observed MJO event, and differ from each other only in the realization of the stochastic parameterizations, applied only in the tropical Indo-Pacific region. Thus even though the errors (deviations within the ensemble) spread globally, they are ultimately due

460 to the uncertainty in this region. These subsequent errors in the tropical diabatic heating, tropical upper-level divergence and Rossby Wave Source indicate the path towards mid-latitude uncertainty in the circulation response.

Caveats to this study include the dependence on the particular model used (the IFS) and the lack of comparison to experiments in which the perturbations were applied more globally. The IFS parameterizes convection and other sub-grid scale processes, possibly accounting for the difference between the tropical error spectra seen in these experiments (Figure 5) and those seen in a convection-resolving model (Judt, 1988). Although we have evidence that the perturbations initially confined to the tropical Indo-Pacific region takes at least 10 days to propagate to other tropical regions (Figure 1, we have not conducted parallel experiments in which the error was applied over a broader band. These await the future.

In conclusion we find that:

- 470 ~~– The uncertainty (average ensemble spread) in total vertically integrated heating exceeds the signal, in part because the detailed evolution of the heating is case-dependent, especially with regard to the state of ENSO is roughly the same magnitude as the MJO signal for the first 5 days, but overtakes the signal subsequently. [Figures 1 and ??Figure 1].~~
- ~~– The propagation of the full Rossby Wave Source is quite coherent in space out to 10 days.[Figure 2]~~
- 475 ~~– The uncertainty of tropical heating is highly scale-dependent: the error on planetary scales has not fully saturated even at the end of the 60-day forecasts, whereas the small scales are fully saturated in about 30 days while the predictability time corresponding to 50% (70%) of saturation in about 25 (45) days. For scales of roughly 1500km (zonal wavenumbers 18-20), those times are reduced to 15 to 20 days. [Figure ??Figures 3 and 4]. Reflecting this, the predictability time  $\tau$  (defined by error reaching half its saturation level)~~
- 480 ~~– While the predictability times for the planetary wave heating is between 24 and and 28 days upper-level divergence are longer than those for diabatic heating (40 to 50 days), the full Rossby Wave Source is less predictable then the heating (planetary wave predictability times of 20 to 30 days). [Table ??, whereas that for the small scale tropical heating is 14 days. The slow growth of errors in the planetary wave heating validates Figure 4]. However this is long enough to validate the application of stationary-wave theory to the extratropical response, as in Matthews et al. (2004)~~
- ~~– The predictability time  $\tau$  for the tropical planetary scale vorticity is about 3 weeks, but is between 15 and and 19 days in mid-latitudes Table ??.~~ The results on the predictability of the Rossby Wave Source are new.
- 485 ~~– The predictability of the planetary wave component of the barotropic Rossby wave source is about 10 days less than that of the tropical heating, indicating that uncertainties in the gradients of planetary wave total vorticity are a factor in limiting extratropical predictability kinetic energy error spectra show the spread of error from the tropics to the sub-tropics, mid-latitudes and high latitude, with the error at a give time decreasing as latitude increases [Table ??Figure 5].~~
- 490 ~~– The role of the stratosphere in amplifying uncertainty is generally confined to the latter part of the 60-day reforecasts, after the ensemble spread in upper-tropospheric heat flux has affected levels above 50 hPa Figures ?? and ??.~~



- 495
- ~~– Ensemble perturbations in both heating and vorticity meridional wind generated over the tropical Indian Ocean amplify first within the tropical band and then propagate amplifies and propagates into the extratropics, reaching a noticeable amplitude over the North Atlantic in the mid-latitude storm tracks after approximately 15 days, after which they amplify its amplifies in situ during the following week [Figures ??–??Figure 6]. Although estimates of such a time lag were already available from observational studies (eg Cassou 2008), the design of our experiments removes the uncertainty associated with the superposition of teleconnections from different parts of the tropical oceans~~
  - ~~– The role of the stratosphere in amplifying uncertainty is generally confined to the latter part of the 60-day reforecasts, after the ensemble spread in upper-tropospheric heat flux has affected levels above 50 hPa [Figures 7 and 8].~~

500 *Code and data availability.* The computer codes used to create the Figures are written in Fortran, and were compiled a recent version of the Intel compiler. They are available from DMS by request. The data from ERA5 reanalysis are from the Computational and Information Systems Laboratory (CISL) of the National Center for Atmospheric Research. Users are required to obtain a Data Analysis Allocation. More information is at : [https://arc.ucar.edu/xras\\_submit/opportunities](https://arc.ucar.edu/xras_submit/opportunities). There were a total of 6 different IFS experiments to generate all the model data that are used in the paper. They are available on the following web pages:

- 505
- <https://doi.org/10.21957/ms6x-gk09>
  - <https://doi.org/10.21957/qtqh-5r32>
  - <https://doi.org/10.21957/tzgp-tv45>
  - <https://doi.org/10.21957/cf3y-0343>
  - <https://doi.org/10.21957/ndqr-vs12>
- 510
- <https://doi.org/10.21957/kt7k-1r77>

The DOIs link to a webpage that provides a description of the available data and retrieval scripts to access the data.

*Author contributions.* The experiments were designed by FM and carried out by SJL, both of whom oversaw the data storage. DMS carried out the analysis to create Figs. 1 through 9, while PY carried out the analysis for Figs. 10 through 12. DD wrote much of the Introduction, while DMS, SJL and PY contributed to the text of the paper. All authors contributed to the discussion of the results and feedback on the manuscript.

515

*Competing interests.* The authors declare no competing interests.

*Acknowledgements.* Support from the Swiss National Science Foundation through project PP00P2\_198896 to P.Y. and D.D. is gratefully acknowledged. The authors also acknowledge suggestions from Kai Huang, and helpful comments from Peter Dueben and Magdalena

Alonso Balmaseda~~-~~, as well as the anonymous reviewers. In addition, Barry Klinger provided valuable help in plotting the data for the  
520 spectra of kinetic energy and heating.

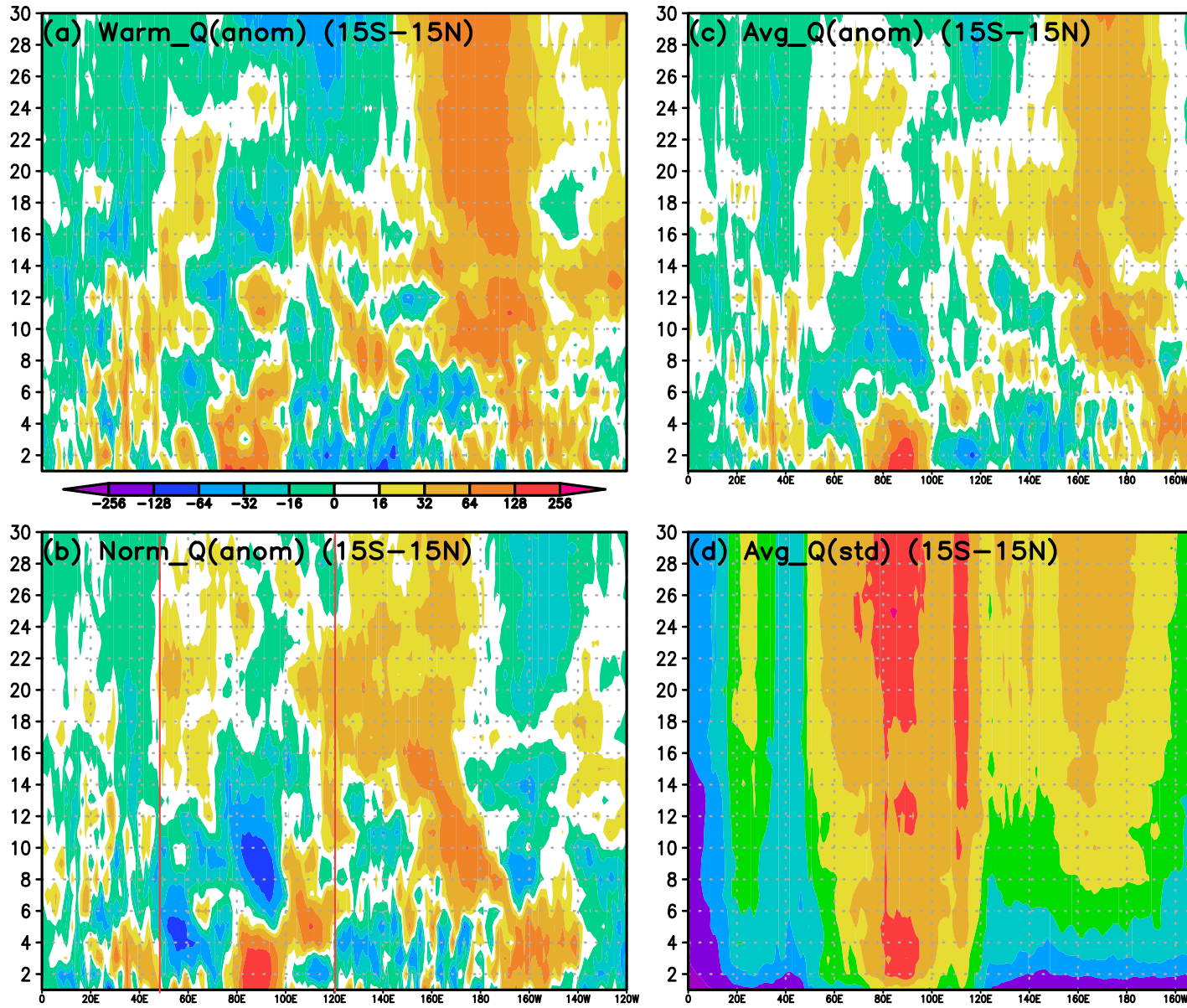


**Figure 1.** (a). Evolution of the daily mean, ensemble mean anomaly of diabatic heating anomaly  $Q$  (vertically integrated and averaged  $15S-15N$   $15^{\circ}S-15^{\circ}N$ ) for days 1-30 of the 60-day experiments, averaged over the four Nov. experiments during warm ENSO events (Nov. 1986, 1987, 2002 and 2015 and Jan. 1987 and 2010). (b) As as in (a), but averaged over the four ENSO-neutral years (1990, 2001, 2004 and 2011) 8 remaining experiments. (c) As in (a), but for the average of all 8 Nov. experiments. (d). The evolution of the ensemble standard deviation of the daily mean heating (vertically integrated and averaged  $15S-15N$   $15^{\circ}S-15^{\circ}N$ ) averaged over all Nov. experiments. The color bar shown in panel (a) applies also to panels (a)-(c). The red lines shown in the panel (b) indicate that range of longitudes over which the stochastic parametrization was applied. Units of  $Wm^{-2}$   $Wm^{-2}$ .

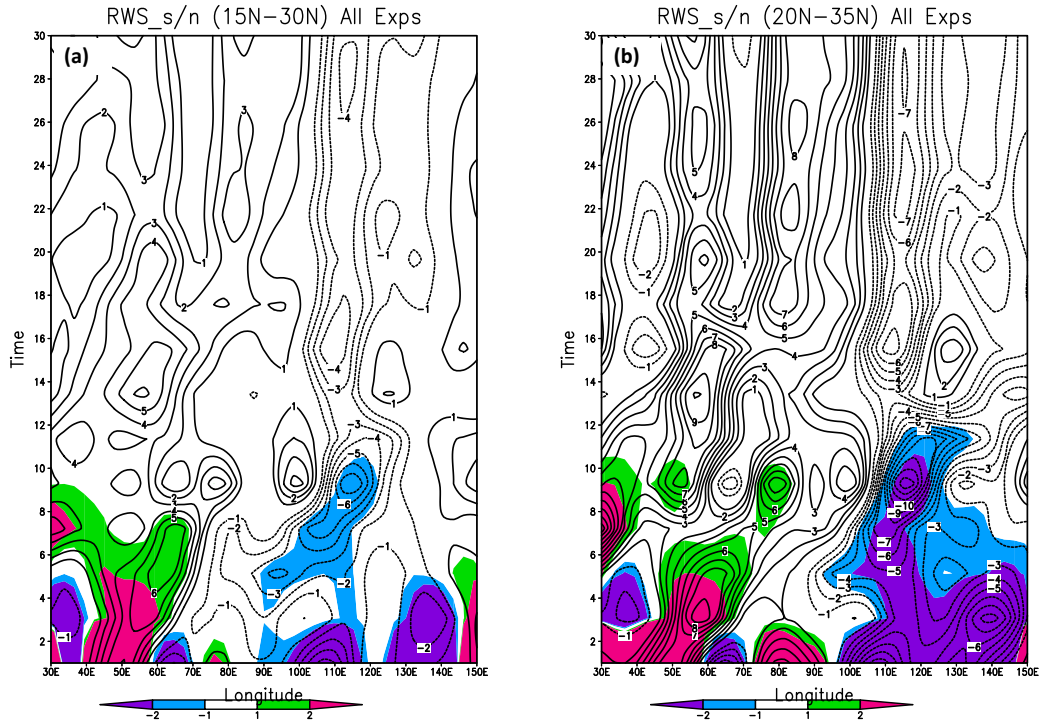


**Figure 2.** (a)-Evolution of the daily-mean, ensemble-mean diabatic heating anomaly-Rossby Wave Source (vertically-integrated and averaged 15S-15N,S) for days 1-30, averaged over the two Jan. all experiments during warm ENSO events (1987 and 2010). (b) As in (a), but averaged over The RWS was computed at the three ENSO-neutral years equivalent of T21 triangular spectral truncation (1990, 1995 and 2013 see text for details). S was averaged between 15° N and 30° N (c) As in (panel a) , but for the average of all five Jan. experiments, and between 20° N and 35° N (d panel b). The evolution of colors scale gives the ensemble standard deviation ratio of the daily-ensemble mean heating (vertically integrated and averaged 15S-15N)-averaged over all Jan. experiments. The color bar shown in panel (a) applies to panels (a)-(c) ensemble spread. The red lines shown in the panel (b) indicate that range-units of longitudes over which the stochastic parametrization was applied RWS are  $ms^{-1}$ . Units of  $Wm^{-2}$ .

(a) Evolution of the Rossby Wave Source (RWS) averaged over the Nov. experiments. The RWS was computed using fields smoothed at the equivalent T21-triangular spectral truncation, and averaged between 15°N and 30°N. See text for details. The

colors scale gives the ratio of the ensemble mean to ensemble spread. (b) Same as in panel (a), but for the Jan. experiments. The units of the RWS are  $m s^{-1}$ .

525 (a) Evolution of error variance of heating  $Q$ , truncated to a T21 representation, in various zonal wavenumber groups averaged over all Nov. experiments, averaged between 15S–15N. Top: zonal waves 1–3. Middle: zonal waves 4–10. Bottom: zonal waves 11–21. Solid red curves: Average variance about the ensemble mean. Solid black curves: Average error with respect to the control run of each ensemble. Solid blue curves: Average error with respect to control runs for many years (estimate of saturation error). (b) Same but for Jan. experiments. Units of  $(W m^{-2})^2$ .

530 (a) Evolution of normalized error variance of heating  $Q$ , truncated to a T21 representation, in various zonal wavenumber groups averaged over all Nov. experiments, averaged between 15S–15N. Top: zonal waves 1–3. Middle: zonal waves 4–10. Bottom: zonal waves 11–21. Solid black curves: Average error with respect to the control run of each ensemble. Solid red curves: Average variance about the ensemble mean. Each curve is normalized by the saturation curve shown in Figure ?? . (b) Same but for Jan. experiments. Units of  $(W m^{-2})^2$ .

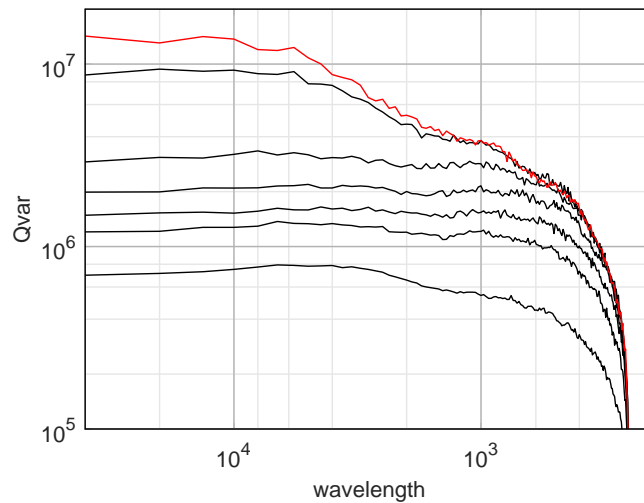


**Figure 3.** Ensemble spread Zonal wavenumber spectra of internal error in mid-level tropical diabatic heating (vertically integrated) averaged over all Nov. experiments  $Q_{mid}$  for various forecast ranges times. Heating has been The heating was averaged over in 2-day blocks, and has been spatially filtered to retain only scales corresponding to T21 truncation was averaged over latitudes  $15^\circ$  S -  $15^\circ$  N. Units of  $Wm^{-2}$ . The color bar in panel six black lines give the spectra (a) applies to all panels. Additional contours starting at 4 (the lowest line) for days 1-2, 8 and 16 are indicated 3-4, 5-6, 9-10, 18-20, 39-40. The heating for days 59-60 is shown in panel (a) the red line. Units of  $log_{10}(Wm^{-2})$ .

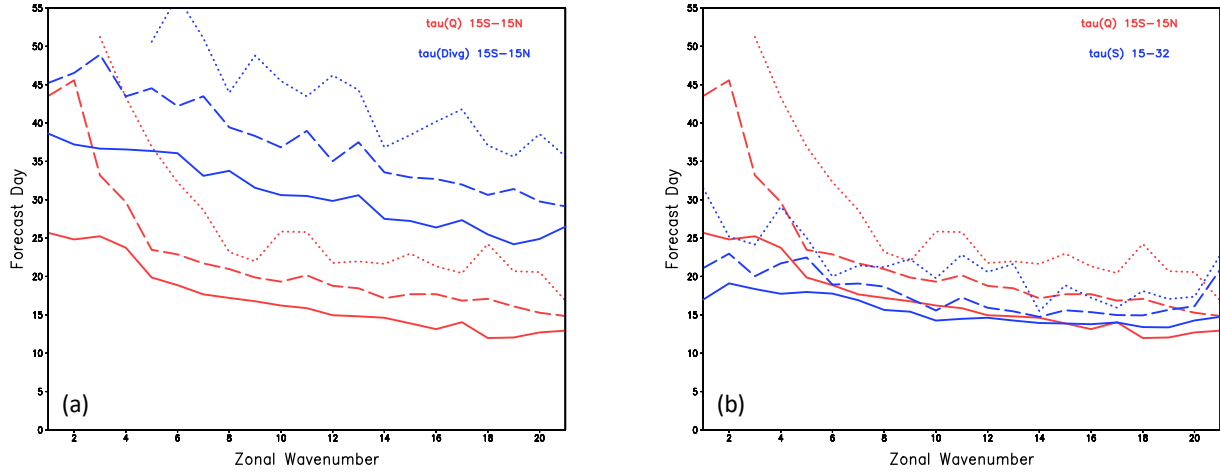


**Figure 4. Ensemble spread** (a) The forecast day  $\tau$  at which the error variance of diabatic heating  $Q$  (vertically integrated) averaged over all Jan. experiments  $15^\circ\text{S} - 15^\circ\text{N}$  reaches a fraction  $f_\tau$  of the external error for various forecast ranges  $f_\tau = 0.50$ . Heating has been averaged over 2-day blocks 0.70 and has been spatially filtered to retain only scales corresponding to T21 truncation 0.90 shown in red solid, dashed and dotted lines. Units of  $Wm^{-2}$ . The color bar in panel blue lines show  $\tau$  for the 200 hPa divergence averaged over the band  $15^\circ\text{S} - 15^\circ\text{N}$ . (ab) applies to all panels. Additional contours at 4, 8 and 16 are indicated  $\tau$  for the error variance in panel heating as in (a) along with  $\tau$  for the Rossby Wave Source ( $S$ ) averaged over  $15^\circ\text{N} - 32^\circ\text{N}$  shown in blue lines.

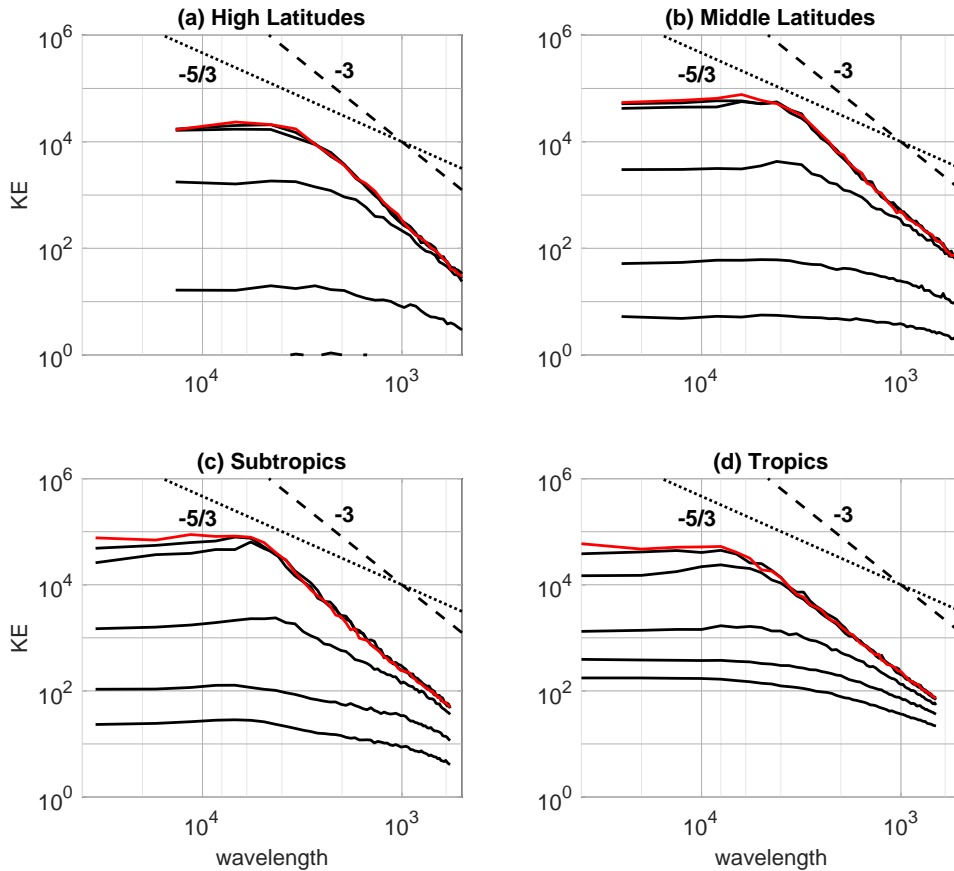


**Figure 5.** Ensemble-spread (a) Error variance spectra of 200–300 hPa vorticity-kinetic energy, averaged over Nov High Latitudes ( $65^{\circ}\text{N} - 75^{\circ}\text{N}$ ), shown at forecast days 3, 5, 10, 20, 30 and 60 (with the 60 day error shown in red). experiments (b) As in (a) but for various forecast ranges Middle Latitudes ( $45^{\circ}\text{N} - 55^{\circ}\text{N}$ ). The vorticity has been averaged over 2-day blocks and has been spatially filtered to retain only scales corresponding to T21 truncation (c) as in (a) but for the Subtropics ( $25^{\circ}\text{N} - 35^{\circ}\text{N}$ ). Units of  $10^{-6}\text{s}^{-1}$ . The color bar (d) as in panel (a) applies but for the Tropics ( $15^{\circ}\text{S} - 15^{\circ}\text{N}$ ). Units of  $\log_{10}(\text{m}^2\text{s}^{-2})$ . Reference spectral slopes corresponding to all panels a  $k^{-5/3}$  and  $k^{-3}$  dependence are indicated



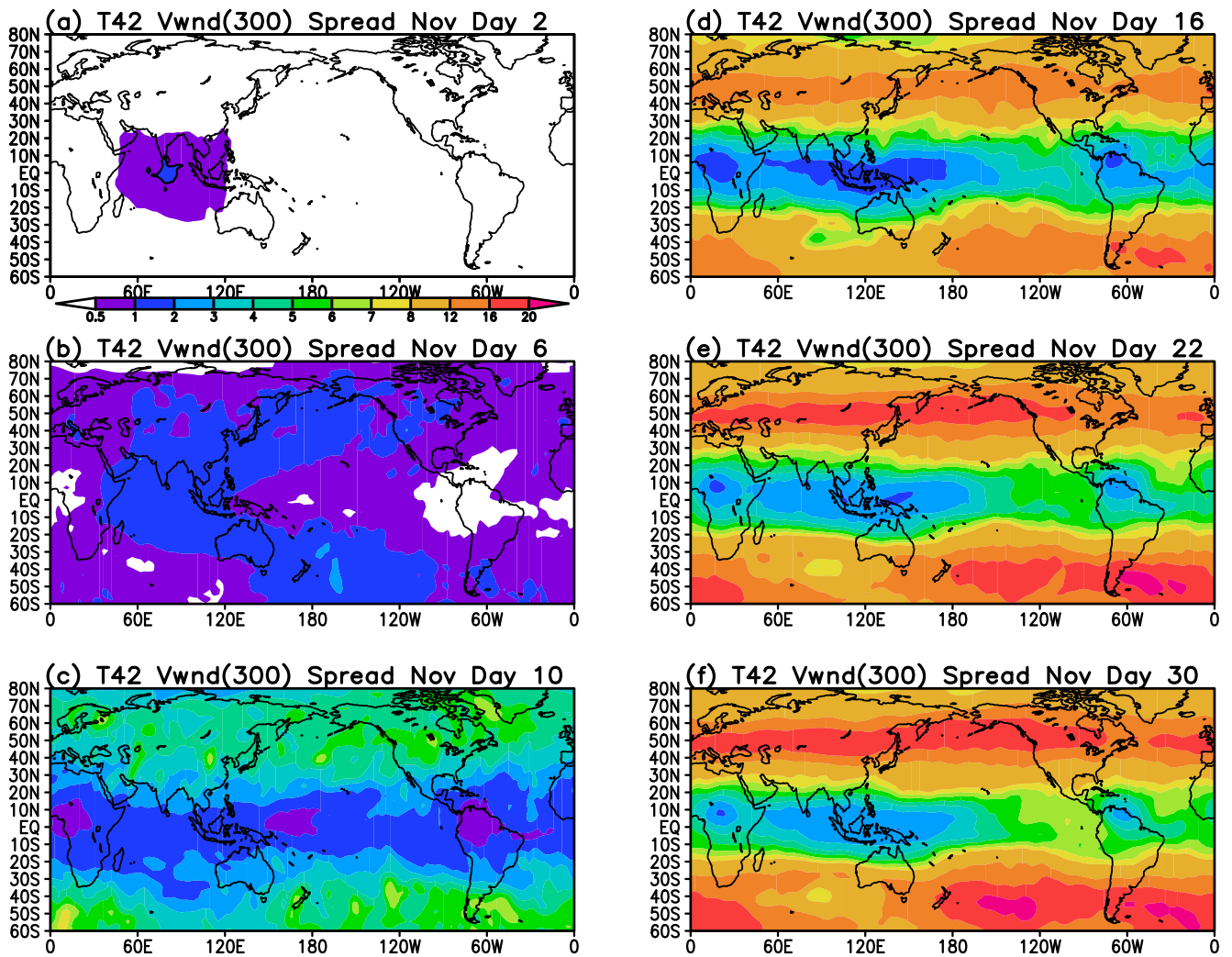


**Figure 6.** Ensemble spread of 200-meridional wind  $v$  at 300 hPa vorticity-averaged-over-Jan. experiments for various forecast ranges. The vorticity has been averaged over 2-day blocks and has been spatially filtered to retain only scales corresponding to T21 truncation. days 2, 6, 10, 16, 22, 30. Units of  $10^{-6} s^{-1}$ . The color bar in panel (a) applies to all panels  $ms^{-1}$ .

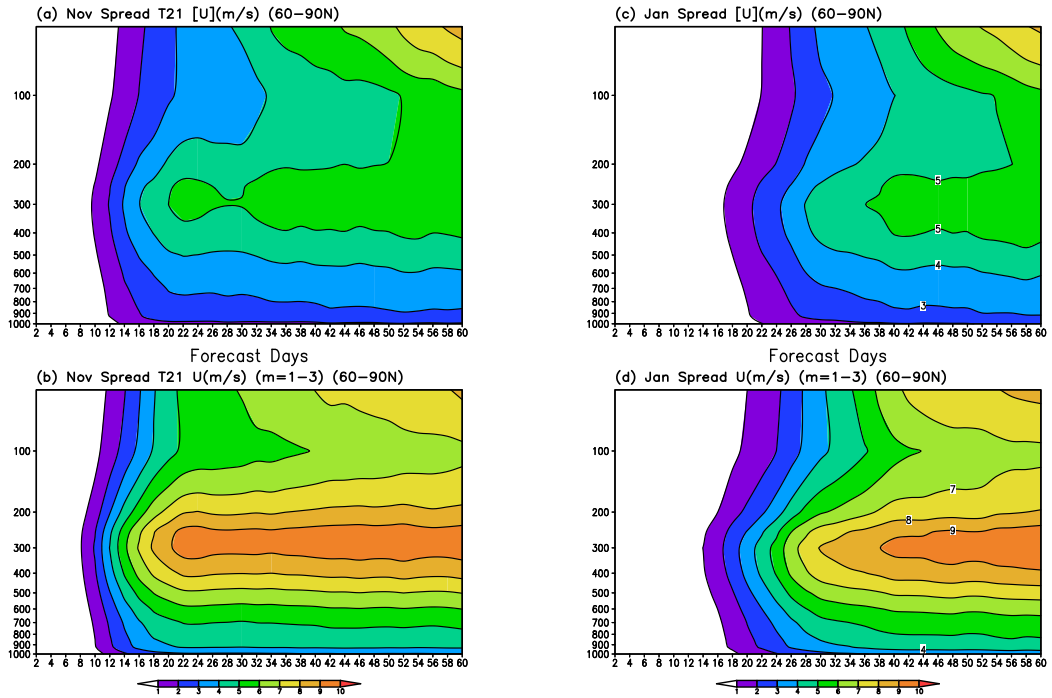


**Figure 7.** Ensemble spread of the zonal wind  $u$ , averaged 60N-90N for all levels (1000 - 50 hPa). The spread of the zonal-mean wind  $[u]$  is shown in panels (a) and (c), and the spread due to zonal wavenumber 1-3 (panels (b) and (d)). The average spread over all Nov. experiments is shown in panels (a) and (b), over all Jan. experiments in panels (c) and (d). Units of  $ms^{-1}$ .

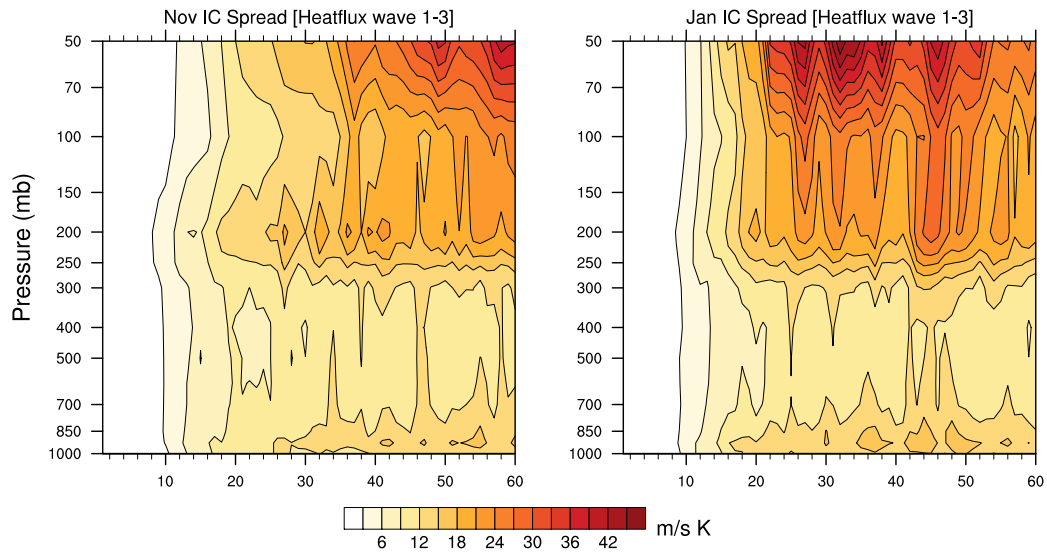


**Figure 8.** Ensemble spread for meridional eddy heat flux (summed over zonal wavenumbers 1 to 3) averaged between 40-80°N for Nov. (left) and Jan. (right) experiments. Units of  $m s^{-1} K$ .

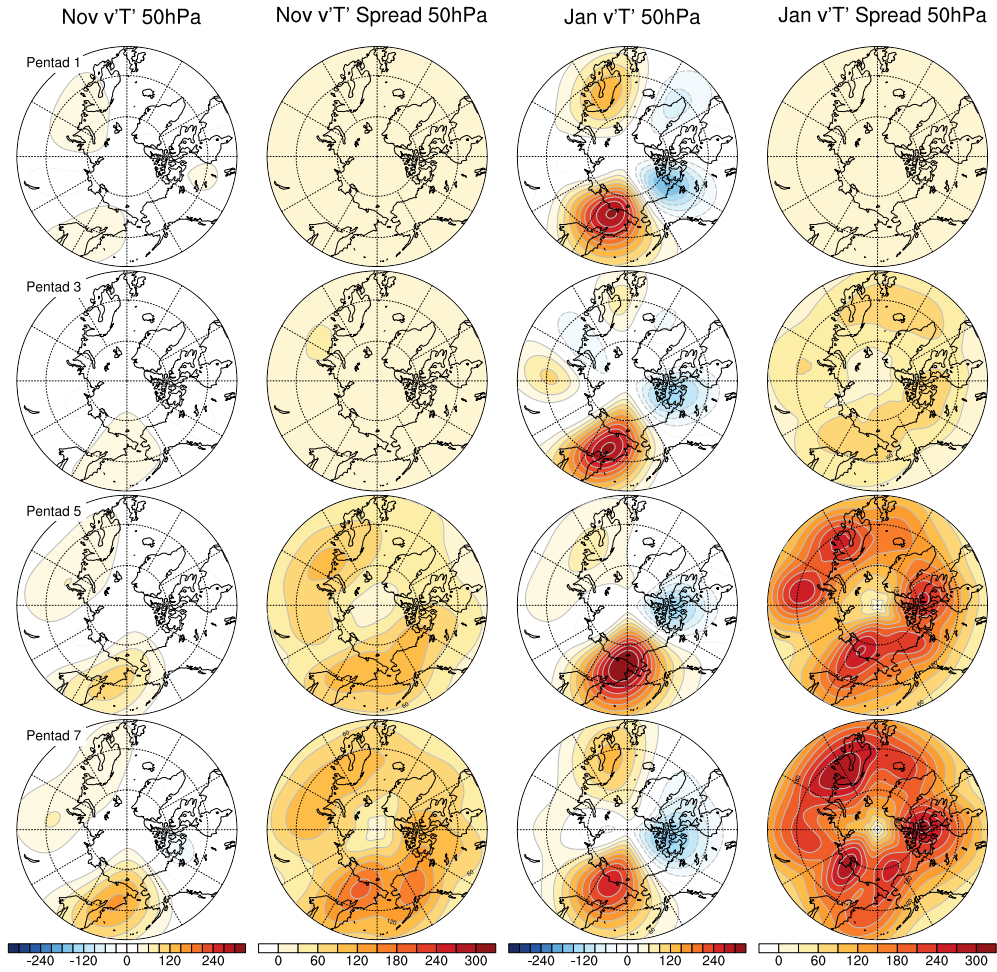


**Figure 9.** Geographical distribution of the planetary wave contribution to the zonal mean ensemble average and ensemble spread of meridional eddy heat flux at 50hPa. The ensemble average is shown in columns 1 and 3, the ensemble spread in columns 2 and 4 (as labeled). Rows 1 - 4 show averages over days 1-5, 11-15, 21-25 and 31-35 respectively. Nov. experiments are given in columns 1 and 2, Jan. results in columns 3 and 4. Contour interval is  $30 \text{ ms}^{-1} \text{ K}$ .

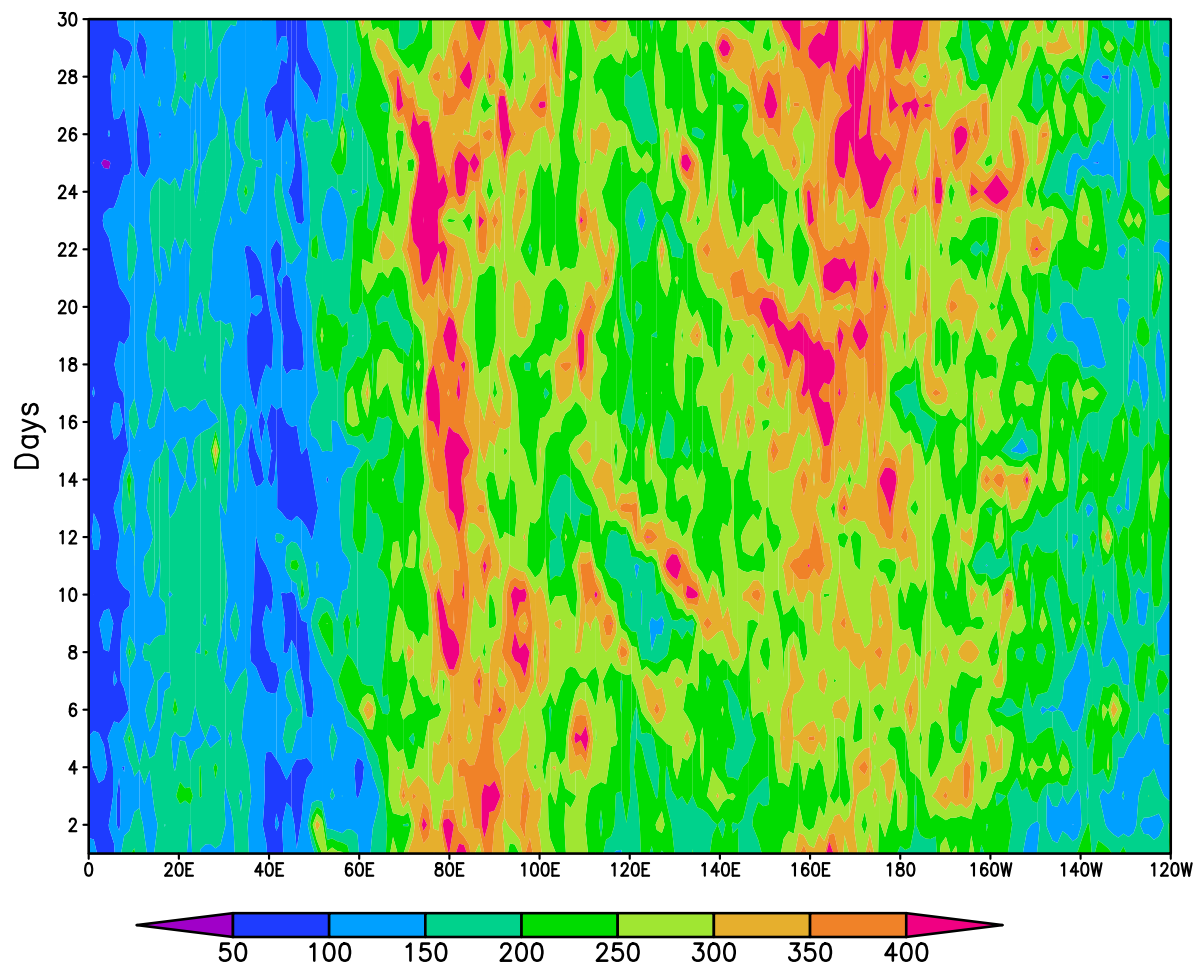


**Figure A1.** Variance of daily mean, vertically integrated diabatic heating (estimated from ERA5 reanalyses for days 1Nov to 30Nov) from the eight years corresponding to the Nov. experiments. See text for details. Units of  $Wm^{-2}$ .

## References

- Ancell, B. C., Bogusz, A., Lauridsen, M. J., and Nauert, C. J.: Seeding Chaos: The Dire Consequences of Numerical Noise in NWP Perturbation Experiments, *Bull. Amer. Meteor. Soc.*, 99, 615–628, 2018.
- Baldwin, M. P. and Dunkerton, T. J.: Stratospheric harbingers of anomalous weather regimes, *Science*, 294, 581–584, 2001.
- 540 Balwin, M. P. and Holton, J. R.: Climatology of the Stratospheric Polar Vortex and Planetary Wave Breaking, *J. Atmos. Sci.*, 45, 1123–1142, 1988.
- Branstator, G. and Teng, H.: Tropospheric Waveguide Teleconnections and Their Seasonality, *J. Atmos. Sci.*, 74, 2017.
- Buizza, R., Miller, M., and Palmer, T. N.: Stochastic representation of model uncertainties in the ECMWF ensemble prediction system, *Q. J. R. Meteorol. Soc.*, 125, 2887–2908, <https://doi.org/10.1002/qj.49712556006>, 1999.
- 545 Camargo, S. J., Wheeler, M. C., and Sobel, A. H.: Diagnosis of the MJO modulation of tropical cyclogenesis using an empirical index, *J. Atmos. Sci.*, 66, 3061–3074, 2009.
- Camargo, S. J., Camp, J., Elsberry, R. L., Gregory, P. A., Klotzbach, P., Schreck, C. J., Sobel, A. H., Ventrice, M. J., Vitart, F., Wang, Z., Wheeler, M. C., Yamaguchi, M., and Zhan, R.: Tropical cyclone prediction on subseasonal time-scales., *Trop. Cyclone Res. Rev.*, 8, 150–165, <https://doi.org/10.1038/j.tccr.2019.10.004>, 2019.
- 550 Cassou, C.: Intraseasonal interaction between the Madden-Julian Oscillation and the North Atlantic Oscillation, *Nature*, 455, 523 – 527, <https://doi.org/10.1038/nature07286>, 2008.
- Charney, J. G.: Geostrophic Turbulence, *J. Atmos. Sci.*, 28, 1087–1095, 1971.
- Dee, D. P. and coauthors: The ERA-Interim reanalysis: configuration and performance of the data assimilation system, *Q. J. R. Meteor. Soc.*, 137, 553–597, 2011.
- 555 Domeisen, D. I., White, C. J., Afargan-Gerstman, H., Muñoz, Á. G., Janiga, M. A., Vitart, F., Wulff, C. O., Antoine, S., Ardilouze, C., Batté, L., et al.: Advances in the subseasonal prediction of extreme events: Relevant case studies across the globe, *Bulletin of the American Meteorological Society*, 2022.
- Domeisen, D. I. V., Butler, A. H., Fröhlich, K., Bittner, M., Müller, W. A., and Baehr, J.: Seasonal predictability over Europe arising from El Niño and stratospheric variability in the MPI-ESM seasonal prediction system, *Journal of Climate*, 28, 256–271, 2015.
- 560 Domeisen, D. I. V., Butler, A. H., Charlton-Perez, A. J., Ayarzagüena, B., Baldwin, M. P., Dunn Sigouin, E., Furtado, J. C., Garfinkel, C. I., Hitchcock, P., Karpechko, A. Y., Kim, H., Knight, J., Lang, A. L., Lim, E.-P., Marshall, A., Roff, G., Schwartz, C., Simpson, I. R., Son, S.-W., and Taguchi, M.: The Role of the Stratosphere in Subseasonal to Seasonal Prediction: 2. Predictability Arising From Stratosphere-Troposphere Coupling, *Journal of Geophysical Research-Atmospheres*, 125, 1–20, 2020a.
- Domeisen, D. I. V., Grams, C. M., and Papritz, L.: The role of North Atlantic-European weather regimes in the surface impact of sudden  
565 stratospheric warming events, *Weather and Climate Dynamics*, 1, 373–388, <https://doi.org/10.5194/wcd-1-373-2020>, 2020b.
- ECMWF: IFS Documentation CY43R3, chap. Part V: Ensemble Prediction System, ECMWF, <https://doi.org/10.21957/vk7qosxn5>, 2017a.
- ECMWF: IFS Documentation CY43R3, chap. Part VII: ECWFM wave model, ECMWF, <https://doi.org/10.21957/mxz9z1gb>, 2017b.
- Ferranti, L., Palmer, T. N., Molteni, F., and Klinker, E.: Tropical-Extratropical Interaction Associated with the 30-60 Day Oscillation and Its Impact on Medium and Extended Range Prediction, *Journal of Atmospheric Sciences*, 47, 2177 – 2199, [https://doi.org/10.1175/1520-0469\(1990\)047<2177:TEIAWT>2.0.CO;2](https://doi.org/10.1175/1520-0469(1990)047<2177:TEIAWT>2.0.CO;2), 1990.
- 570 Garfinkel, C. I. and Schwartz, C.: MJO-Related Tropical Convection Anomalies Lead to More Accurate Stratospheric Vortex Variability in Subseasonal Forecast Models, *Geophysical Research Letters*, 44, 10,054–10,062, <https://doi.org/10.1002/2017GL074470>, 2017.

- Garfinkel, C. I., Benedict, J. J., and Maloney, E. D.: Impact of the MJO on the boreal winter extratropical circulation, *Geophysical Research Letters*, 41, 6055–6062, 2014.
- 575 Garfinkel, C. I., W. Chen, W., Li, Y., C. Schwartz, C., Yadav, P., and Thompson, D.: The Winter North Pacific Teleconnection in Response to ENSO and the MJO in Operational Subseasonal Forecasting Models is Too Weak, *J. Clim.*, 35, 4413–4430, 2022.
- Goosse, H. and Fichefet, T.: Importance of ice-ocean interactions for the global ocean circulation: A model study, *Journal of Geophysical Research: Oceans*, 104, 23 337–23 355, <https://doi.org/10.1029/1999JC900215>, 1999.
- Hall, J. D., Matthews, A. J., and Karoli, D. J.: The modulation of tropical cyclone activity in the Australian region by the Madden-Julian  
580 Oscillation, *Mon. Wea. Rev.*, 129, 2970–2982, 2001.
- Hersbach, H. and coauthors: The ERA5 global reanalysis, *Q. J. R. Meteorol. Soc.*, 146, 199 – 2049, <https://doi.org/10.1002/qj.3803>, 2020.
- Jones, C., Waliser, D. E., Lau, K. M., and Stern, W.: Global Occurrences of Extreme Precipitation and the Madden-Julian Oscillation: Observations and Predictability, *Journal of Climate*, 17, 4575–4589, <https://doi.org/10.1175/3238.1>, 2004.
- Judt, F.: Atmospheric Predictability of the Tropics, Middle Latitudes, and Polar Regions Explored through Global Storm-Resolving Simula-  
585 tions, *J. Atmos. Sci.*, 77, 257–275, 1988.
- Judt, F.: Insights into atmospheric predictability through global convection-permitting model simulations., *J. Atmos. Sci.*, 75, 1477–1497, <https://doi.org/https://doi.org/10.1175/JAS-D-17-0343.1>, 2018.
- Kang, W. and Tziperman, E.: The MJO-SSW Teleconnection: Interaction Between MJO-Forced Waves and the Midlatitude Jet, *Geophys. Res. Lett.*, 45, 4400–4409, <https://doi.org/https://doi.org/10.1029/2018GL077937>, 2018.
- 590 Kosovelj, K., a. F. K., Molteni, F., and Zagar, N.: Modal Decomposition of the Global Response to Tropical Heating Perturbations Resembling MJO., *J. Atmos. Sci.*, 76, 1457–1469, 2019.
- Lee, C.-Y., Camargo, S. J., Vitart, F., Sobel, A. H., and Tippett, M. K.: Subseasonal Tropical Cyclone Genesis Prediction and MJO in the S2S Dataset, *Wea. Forecasting*, 33, 967 – 988, <https://doi.org/10.1175/WAF-D-17-0165.1>, 2018.
- Lee, R. W., Woolnough, S. J., Charlton-Perez, A. J., and Vitart, F.: ENSO Modulation of MJO Teleconnections to the North Atlantic and  
595 Europe, *Geophysical Research Letters*, 46, 13 535 – 13 545, <https://doi.org/10.1029/2019GL084683>, 2019.
- Leroy, A. and Wheeler, M. C.: Statistical prediction of weekly tropical cyclone activity in the southern hemisphere, *Mon. Wea. Rev.*, 136, 3637–3654, 2008.
- Leutbecher, M., Lock, S.-J., Ollinaho, P., Lang, S. T. K., Balsamo, G., Bechtold, P., Bonavita, M., Christensen, H. M., Diamantakis, M.,  
Dutra, E., English, S., Fisher, M., Forbes, R. M., Goddard, J., Haiden, T., Hogan, R. J., Juricke, S., Lawrence, H., MacLeod, D.,  
600 Magnusson, L., Malardel, S., Massart, S., Sandu, I., Smolarkiewicz, P. K., Subramanian, A., Vitart, F., Wedi, N., and Weisheimer, A.: Stochastic representations of model uncertainties at ECMWF: state of the art and future vision, *Q. J. R. Meteorol. Soc.*, 143, 2315–2339, <https://doi.org/10.1002/qj.3094>, 2017.
- Li, Z., Peng, J., and Zhang, L.: Spectral budget of Rotational and Divergent Kinetic Energy in Global Analyses, *J. Atmos. Sci.*, 80, 813–831,  
2023.
- 605 Lin, H. and Brunet, G.: The influence of the Madden-Julian oscillation on Canadian wintertime surface air temperature, *Monthly Weather Review*, 137, 2250–2262, 2009.
- Lin, H., Brunet, G., and Derome, J.: An Observed Connection between the North Atlantic Oscillation and the Madden-Julian Oscillation, *Journal of Climate*, 22, 364 – 380, <https://doi.org/10.1175/2008JCLI2515.1>, 2009.
- Lin, H., Brunet, G., and Fontecilla, J. S.: Impact of the Madden-Julian Oscillation on the intraseasonal forecast skill of the North Atlantic  
610 Oscillation, *Geophysical Research Letters*, 37, <https://doi.org/10.1029/2010GL044315>, 2010.

- Liu, J., Da, Y., Li, T., and Hu, F.: Impact of ENSO on MJO Pattern Evolution over the Maritime Continent, *J. Meteor. Res.*, 34, 1151–1166, 2020.
- Madden, R. A. and Julian, P. R.: Detection of a 40–50 day oscillation in the zonal wind in the tropical Pacific, *Journal of Atmospheric Sciences*, 28, 702–708, 1971.
- 615 Madden, R. A. and Julian, P. R.: Description of global-scale circulation cells in the tropics with a 40–50 day period, *Journal of Atmospheric Sciences*, 29, 1109–1123, 1972.
- Madec, G. and the NEMO team: NEMO ocean engine, Notes du Pôle de modélisation de l’Institut Pierre-Simon Laplace (IPSL), pp. 915–934, <https://doi.org/10.5281/zenodo.1475234>, 2013.
- Maloney, E. D. and Hartmann, D. L.: Modulation of hurricane activity in the Gulf of Mexico by the Madden-Julian oscillation, *Science*, 287, 620 2002–2004, 2000.
- Matthews, A. J., Hoskins, B. J., and Masutani, M.: The global response to tropical heating in the Madden-Julian oscillation during the northern winter, *Q. J. R. Meteorol. Soc.*, 130, 1991 – 2011, <https://doi.org/10.1017/qj.2004.02.123>, 2004.
- Merryfield, W. J., Baehr, J., Batté, L., Becker, E. J., Butler, A. H., Coelho, C. A. S., Danabasoglu, G., Dirmeyer, P. A., Doblas-Reyes, F. J., Domeisen, D. I. V., Ferranti, L., Ilynia, T., Kumar, A., Müller, W. A., Rixen, M., Robertson, A. W., Smith, D. M., Takaya, Y., Tuma, 625 M., Vitart, F., White, C. J., Alvarez, M. S., Ardilouze, C., Attard, H., Baggett, C., Balmaseda, M. A., Beraki, A. F., Bhattacharjee, P. S., Bilbao, R., de Andrade, F. M., DeFlorio, M. J., Díaz, L. B., Ehsan, M. A., Fragkoulidis, G., Grainger, S., Green, B. W., Hell, M. C., Infanti, J. M., Isensee, K., Kataoka, T., Kirtman, B. P., Klingaman, N. P., Lee, J.-Y., Mayer, K., McKay, R., Mecking, J. V., Miller, D. E., Neddermann, N., Justin Ng, C. H., Osso, A., Pankatz, K., Peatman, S., Pegion, K., Perlwitz, J., Recalde-Coronel, G. C., Reintges, A., Renkl, C., Solaraju-Murali, B., Spring, A., Stan, C., Sun, Y. Q., Tozer, C. R., Vigaud, N., Woolnough, S., and Yeager, S.: Current and 630 Emerging Developments in Subseasonal to Decadal Prediction, *Bulletin of the American Meteorological Society*, 101, E869–E896, 2020.
- Muñoz, Á. G., Goddard, L., Mason, S. J., and Robertson, A. W.: Cross-time scale interactions and rainfall extreme events in southeastern South America for the austral summer. Part II: Predictive skill, *Journal of Climate*, 29, 5915–5934, 2016.
- Rodney, M., Lin, H., and Derome, J.: Subseasonal Prediction of Wintertime North American Surface Air Temperature during Strong MJO Events, *Monthly Weather Review*, 141, 2897–2909, 2013.
- 635 Sardeshmukh, P. D. and Hoskins, B. J.: The generation of global rotational flow by steady idealized tropical divergence, *Journal of the Atmospheric Sciences*, 45, 1228–1251, 1988.
- Schwartz, C. and Garfinkel, C. I.: Troposphere-Stratosphere Coupling in Subseasonal-to-Seasonal Models and its Importance for a Realistic Extratropical Response to the Madden-Julian Oscillation, *Journal of Geophysical Research: Atmospheres*, 125, e2019JD032043, 2020.
- Schwartz, C., Garfinkel, C. I., Yadav, P., Chen, W., and Domeisen, D. I. V.: Stationary wave biases and their effect on upward troposphere– 640 stratosphere coupling in sub-seasonal prediction models, *Weather and Climate Dynamics*, 3, 679–692, <https://doi.org/10.5194/wcd-3-679-2022>, 2022.
- Selz, T.: Estimating the Intrinsic Limit of Predictability Using a Stochastic Convection Scheme, *J. Atmos. Sci.*, 76, 757 – 765, 2019.
- Stan, C., Straus, D. M., Frederiksen, J. S., Lin, H., Maloney, E. D., and Schumacher, C.: Review of tropical-extratropical teleconnections on intraseasonal time scales, *Reviews of Geophysics*, 55, 902–937, 2017.
- 645 Stan, C., Zheng, C., Chang, E. K.-M., Domeisen, D. I., Garfinkel, C. I., Jenney, A. M., Kim, H., Lim, Y.-K., Lin, H., Robertson, A., et al.: Advances in the prediction of MJO-Teleconnections in the S2S forecast systems, *Bulletin of the American Meteorological Society*, 2022.
- Straus, D. M.: On the role of the seasonal cycle, *J. Atmos. Sci.*, 40, 303 – 313, 1983.



- Straus, D. M. and Paolino, D.: Intermediate time error growth and predictability: tropics versus mid-latitudes, *Tellus A*, 61, 579 – 586, <https://doi.org/10.1111/j.1600-0870.2009.00411.x>, 2009.
- 650 Straus, D. M., Swenson, E., and Lappen, C.-L.: The MJO Cycle Forcing of the North Atlantic Circulation: Intervention Experiments with the Community Earth System Model, *J. Atmos. Sci.*, 72, 660 – 681, <https://doi.org/10.1175/JAS-D-14-0145.1>, 2015.
- Sun, Y. Q., Rotunno, R., and Zhang, F.: Contributions of Moist Convection and Internal Gravity Waves to Building the Atmospheric -5/3 Kinetic Energy Spectra, *J. Atmos. Sci.*, 74, 185 – 201, 2017.
- Swenson, E. T. and Straus, D. M.: A modelling framework for a better understanding of the tropically-forced component of the Indian monsoon variability, *J. Earth Syst. Sci.*, 130, <https://doi.org/10.1007/s12040-020-01503-z>, 2021.
- 655 Valadão, C. E., Carvalho, L. M., Lucio, P. S., and Chaves, R. R.: Impacts of the Madden-Julian oscillation on intraseasonal precipitation over Northeast Brazil, *International Journal of Climatology*, 37, 1859–1884, 2017.
- Vitart, F.: Evolution of ECMWF sub-seasonal forecast skill scores, *Q. J. R. Meteorol. Soc.*, 140, 1889 – 1899, <https://doi.org/10.1002/qj.2256>, 2014.
- 660 Vitart, F.: Madden-Julian Oscillation prediction and teleconnections in the S2S database, *Q. J. R. Meteorol. Soc.*, 143, 2210–2220, 2017.
- Vitart, F., Ardilouze, C., Bonet, A., Brookshaw, A., Chen, M., Codorean, C., Déqué, M., Ferranti, L., Fucile, E., Fuentes, M., et al.: The subseasonal to seasonal (S2S) prediction project database, *Bulletin of the American Meteorological Society*, 98, 163–173, 2017.
- Wang, J., Kim, H., Kim, D., Henderson, S. A., Stan, C., and Maloney, E. D.: MJO teleconnections over the PNA region in climate models. Part II: Impacts of the MJO and basic state, *Journal of Climate*, 33, 5081–5101, 2020.
- 665 Wheeler, M. C. and Hendon, H. H.: An All-Season Real-Time Multivariate MJO Index: Development of an Index for Monitoring and Prediction, *Mon. Wea. Rev.*, 132, 1917 – 1932, [https://doi.org/10.1175/1520-0493\(2004\)132<1917:AARMMI>2.0.CO;2](https://doi.org/10.1175/1520-0493(2004)132<1917:AARMMI>2.0.CO;2), 2004.
- Yadav, P. and Straus, D. M.: Circulation Response to Fast and Slow MJO Episodes, *Monthly Weather Review*, 145, 1577 – 1596, <https://doi.org/10.1175/MWR-D-16-0352.1>, 2017.
- Zagar, N., Jelic, D., Blaauw, M., and Bechtold, P.: Energy Spectra and Inertia-Gravity Waves in Global Analyses, *J. Atmos. Sci.*, 74, 2447 – 2466, 2017.
- 670 Zhang, Y., Sun, Y. Q., Magnusson, L., Buizza, R., Lin, S.-J., Chen, J.-H., and Emanuel, K.: What is the Predictability Limit of Midlatitude Weather?, *J. Atmos. Sci.*, 76, 1077–1089, 2019.
- Zhao, Y.-B., Zagar, N., Lunkeit, F., and Blender, R.: Atmospheric bias teleconnections associated with systematic SST errors in the tropical Indian Ocean, *Weather and Climate Dynamics*, <https://doi.org/10.5194/egusphere-2023-917>, 2023.